Small-scale convection in a plume-fed low-viscosity layer beneath a moving plate

Roberto Agrusta, Diane Arcay, Andrea Tommasi, Anne Davaille, Neil Ribe, Taras Gerya

Geophysical Journal International

Geophys. J. Int. (2013) **194,** 591–610
Advance Access publication 2013 April 23

doi: 10.1093/gji/ggt128

Small-scale convection in a plume-fed low-viscosity layer beneath a moving plate

Roberto Agrusta,[1] Diane Arcay,[1] Andréa Tommasi,[1] Anne Davaille,[2] Neil Ribe[2] and Taras Gerya[3]

[1] *Geosciences Montpellier, CNRS & Université de Montpellier* 2, F-34095 *Montpellier Cedex 5, France. E-mail: roberto.agrusta@gm.univ-montp2.fr*
[2] *Laboratoire Fluides, Automatique et Systèmes Thermiques (FAST), CNRS & Université Paris* 11*, Orsay, France*
[3] *Swiss Federal Institute of Technology Zurich, Department of Geosciences, Zürich, Switzerland*

Accepted 2013 March 28. Received 2013 March 28; in original form 2012 August 06

SUMMARY

Two-dimensional simulations using a thermomechanical model based on a finite-difference method on a staggered grid and a marker in cell method are performed to study the plume–lithosphere interaction beneath moving plates. The plate and the convective mantle are modelled as a homogeneous peridotite with a Newtonian temperature- and pressure-dependent viscosity. A constant velocity, ranging from 5 to 12.5 cm yr^{-1}, is imposed at the top of the plate. Plumes are generated by imposing a thermal anomaly of 150 to 350 K on a 50 km wide domain at the base of the model (700 km depth); the plate atop this thermal anomaly is 40 Myr old. We analyse (1) the kinematics of the plume as it impacts the moving plate, (2) the dynamics of time-dependent small-scale convection (SSC) instabilities developing in the low-viscosity layer formed by spreading of hot plume material at the base of the lithosphere and (3) the resulting thermal rejuvenation of the lithosphere. The spreading of the plume material at the base of the lithosphere, characterized by the ratio between the maximum down- and upstream horizontal (dimensionless) velocities in the plume-fed sublithospheric layer, $Pe_{\rm up}/Pe_{\rm down}$ depends on the ratio between the maximum plume upwelling velocity and the plate velocity, $Pe_{\rm plume}/Pe_{\rm plate}$. For fast plate velocities and sluggish plumes (low $Pe_{\rm plume}/Pe_{\rm plate}$), plate motion drags most plume material and downstream flow is dominant. As $Pe_{\rm plume}/Pe_{\rm plate}$ increases, an increasing part of the plume material flows upstream. SSC systematically develops in the plume-fed sublithospheric layer, downstream from the plume. Onset time of SSC decreases with the Rayleigh number. For vigorous plumes, it does not depend on plate velocity. For more sluggish plumes, however, variations in the plume spreading behaviour at the base of the lithosphere result in a decrease in the onset time of SSCs with increasing plate velocity. In any case, SSC results in uplift of the isotherm 1573 K by up to 20 km relative to its initial equilibrium depth at the impact point.

Key words: Mantle processes; Dynamics of lithosphere and mantle; Dynamics: convection currents, and mantle plumes; Hotspots; Rheology: mantle.

1 INTRODUCTION

Mantle plumes are supposed to produce rejuvenation and bottom-up thinning of the impacted lithosphere, playing an essential role in the initiation of rifting (e.g. Courtillot *et al.* 1999). Yet, the extent and rates of erosion of the base of a moving plate atop a mature mantle plume remain poorly constrained. Interactions between the plume and the base of the lithosphere are evidenced by topography and geoid swells. These observations integrate, however, the contribution of the buoyant plume material at sublithospheric depths, the dynamic topography associated with the plume upwelling, and the lithosphere erosion by the plume (Ribe & Christensen 1994).

Seismic data, in particular receiver functions, may be used to probe the topography of the lithosphere–asthenosphere boundary (LAB) atop mantle plumes and hence to evaluate the lithosphere erosion. However, results for different methods and hotspots vary strongly. The shear wave velocity structure of the uppermost mantle beneath both the Galapagos and the Cape Verde archipelagoes is characterized by a high-velocity lid of variable thickness beneath the different islands (between 40 and 70 km in Galapagos and 80 and 110 km in Cape Verde) underlain by a low-velocity asthenosphere (Lodge & Helffrich 2006; Villagomez *et al.* 2007). *P*- and *S*-wave tomography models beneath the Hawaiian island chain show low-velocity anomalies in the upper 200 km of the mantle depth, but no clear lithospheric thinning (Wolfe *et al.* 2009, 2011). In contrast, *S*-wave receiver function data beneath Hawaii show a gradual thinning of the lithosphere from the Big Island, where the lithosphere is 100 km thick, towards Kauai, 500 km downstream from

the present location of the plume, where the LAB is mapped at ∼50 km depth (Li *et al.* 2004). Surface wave velocity tomography images a pronounced low-velocity anomaly in the asthenosphere that is centred to the west of the island of Hawaii and a less marked, 200 km wide, low-velocity anomaly at shallower depths (<60 km); the latter is stronger between Hawaii and Maui (Laske *et al.* 2011). Finally, underside reflection data imply that the Pacific lithosphere thins by ∼10 km along the Hawaiian chain over a lateral scale of ∼1000 km (Schmerr 2012). A recent gravity study in Hawaii, using a method based on a continuous wavelet transform, shows that the geoid-to-topography ratio varies along the swell, from 8 m km^{-1} on Big Island to 6 m km^{-1} on Kauai. This decrease indicates a decay of the average depth of compensation by 20 km (Cadio *et al.* 2012), further hinting for increased lithosphere thinning beneath Kawaii.

Numerical models show that lithospheric thinning by heat conduction above a mantle plume is a slow process that it is limited to the time span during which the plate remains over the plume; motion of plate away from the hotspot results in re-thickening of lithosphere by conductive cooling (Crough & Thompson 1976; Crough 1978; Detrick & Crough 1978; Sphon & Schubert 1982; Monnereau *et al.* 1993; Ribe 2004). In these models, a plume impacting a fast-moving lithosphere results in very limited thinning. Development of gravitational instabilities or small-scale convection (SSC) in the low-viscosity layer formed by the spreading of the hot plume material at the base of the lithosphere may, on the other hand, effectively erode the lithosphere, even for a fast-moving plate like the Pacific (Sleep 1994; Moore *et al.* 1998; Thoraval *et al.* 2006). These models predict that the maximum thinning is offset from the plume impact point. Recent 3-D models show that SSC also results in additional decompression melting, explaining the secondary volcanism occurring a few m.y. after the main volcanic activity in hotspots like Hawaii (Ballmer *et al.* 2011). These studies analysed, however, a limited range of plumes and plate velocities and scaling laws relating the time of onset of SSC after the plume impact to the Rayleigh number in the plume-fed sublithospheric layer could not be determined. These scaling laws are essential for comparing this system and the SSC occurring beneath a rigid lid cooling from the surface, which has been extensively studied in the last 30 yr (e.g. Fleitout & Yuen 1984; Davaille & Jaupart 1993, 1994; Doin *et al.* 1997; Choblet & Sotin 2000; Korenaga & Jordan 2002, 2003; Huang *et al.* 2003; Dumoulin *et al.* 2005; Ballmer *et al.* 2009).

The purpose of this paper is to study the effects of the plume vigour, which depends on the plume buoyancy and on the mantle viscosity, and of the plate velocity on the dynamics of the SSC produced by the spreading of hot plume material at the base of the lithosphere. We also investigate the effect of these parameters on the initial spreading of the plume material at the base of the plate, that is, on the relative proportion of upstream (towards the ridge) and downstream flow. Finally, we analyse the role of these two processes on the thermomechanical erosion of the base of the lithosphere atop a plume.

2 MODEL SETUP

We use the 2-D thermomechanical thermal code I2VIS (Gerya & Yuen 2003), based on a finite-difference scheme and a marker in-cell method, to simulate the plume–lithosphere interaction beneath a moving plate. The code solves on a staggered grid the equations of conservation of mass, momentum and energy for a fluid assumed to be incompressible, except for the thermal expansion and compressibility terms in the momentum equation. Radiogenic, adiabatic and shear heating productions are neglected. The marker-in-cell method is used to model the advection term in the heat equation; this prevents numerical diffusion. The material properties, such as density, viscosity and thermal conductivity, are attributed to Lagrangian points (markers), which are advected according to the velocity field using a fourth order in space/first order in time explicit Runge–Kutta scheme. The advected properties are then linearly interpolated from the Lagrangian markers to the Eulerian mesh.

The modelled domain is 4000 km wide and 700 km high (Fig. 1). The simulation box has a homogeneous peridotite composition, whose density and viscosity vary as a function of depth and temperature. Mechanical boundary conditions are free slip along the left and top boundaries. The open bottom and right boundaries have an external no slip condition (Gerya *et al.* 2008), implemented by limiting the velocity components at the bottom as:

$$\partial V_x / \partial y = -V_x / \Delta y_{\text{external}} \quad \text{and} \quad \partial V_y / \partial y = -V_y / \Delta y_{\text{external}}, \tag{1}$$

and at the right boundary as

$$\partial V_x / \partial x = -V_x / \Delta x_{\text{external}} \quad \text{and} \quad \partial V_y / \partial x = -V_y / \Delta y_{\text{external}}, \tag{2}$$

where $\Delta y_{\text{external}}$ and $\Delta x_{\text{external}}$ are, respectively, the distances between the bottom and the right side of the model to the points where a no slip condition ($V_x = 0$, $V_y = 0$) is satisfied. The conditions (1) and (2) impose a constant velocity gradient at the boundary, controlled by the Δ_{external}. A real natural open boundary, simulated by a constant flux, is reproduced if Δ_{external} is infinite. In the present models, to ensure numerical stability, semi-natural open boundary is modelled by imposing very low-velocity gradients normal to the bottom and right-lateral open boundaries, $\Delta y_{\text{external}}$ and $\Delta x_{\text{external}}$ being set to 7368 and 9389 km, respectively. The plate velocity is imposed by applying a constant horizontal velocity, V_{plate}, at 10 km depth from $x = -1980$ km to $x = 1970$ km (Fig. 1a).

Constant temperatures T_0 and T_1 (273 and 1623 K) are imposed on the top and bottom boundaries, respectively. The bottom temperature is homogeneous (that is, models are run without plumes) until thermal equilibrium, characterized by a constant heat flux across the lithosphere over the last 500 km of the box is reached. A null horizontal heat flow is imposed on the lateral boundaries. The initial temperature field at plume initiation (Fig. 1b) represents therefore an oceanic plate cooling away from a ridge located at the top left corner of the model (at $x = -2000$ km). In order to obtain a lithosphere aged of 40 Myr at the middle of the box (at $x = 0$ km) for all plate velocities, the thermal conductivity in the first 150 km of the model (k_0) is increased accordingly to

$$k_0 = k \left(age - \frac{X_1}{V_{\text{plate}}} \right) \frac{V_{\text{plate}}}{X_0}, \tag{3}$$

where k is the thermal conductivity of the upper mantle, set to 3.2 W m^{-1} K^{-1}, *age* is 40 Myr, X_0 is 150 km, X_1 is 1850 km and V_{plate} is the plate velocity (Fig. 1b). Tests on the effect of this laterally varying thermal diffusivity show that increasing both vertical and horizontal heat flux in leftmost 150 km of the model domain does not significantly affect the thermal structure of the lithosphere in the area where the plume impinges and interacts with its base (Appendix A). The only notable difference is the slightly younger lithosphere age (isotherms are ∼2 km shallower) in the case where the approximation (3) is used.

Once thermal equilibrium is achieved (t_{init}, usually after ∼150 Myr), a plume is generated by modifying the bottom

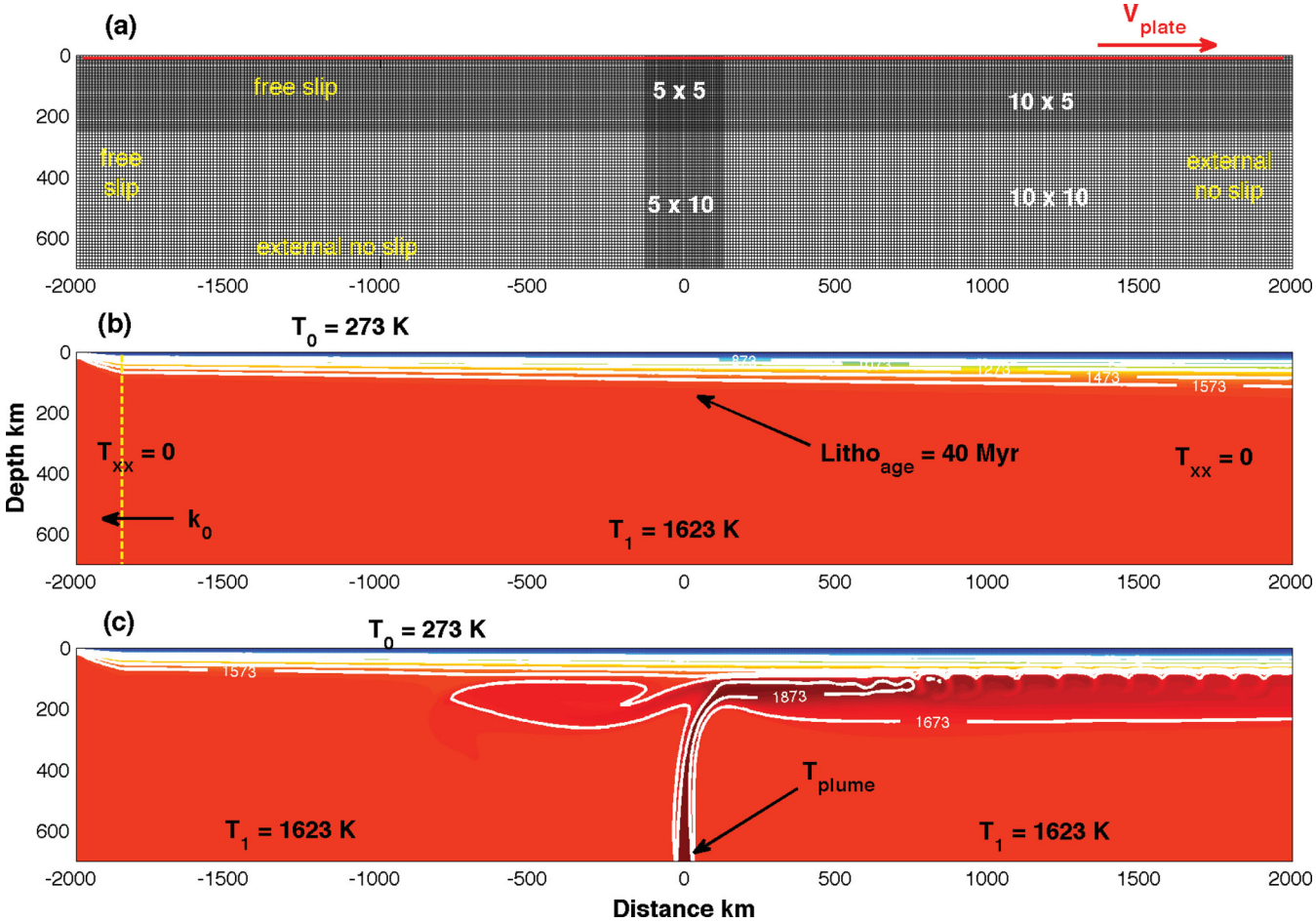

Figure 1. 2-D numerical setup. (a) Geometry of numerical grid and mechanical boundary conditions. (b) Initial thermal boundary conditions and temperature field at time $t_{\rm init}$, when the thermal plume is introduced. (c) Thermal boundary conditions generating and sustaining stable plumes at times higher than $t_{\rm init}$. Simulation 31 with a plume characterized by a $\Delta T_{\rm plume}$ of 300 K impinging a plate moving at 10 cm yr^{-1}.

boundary conditions: a temperature anomaly, defined as $T_{\rm plume} = \Delta T_{\rm plume} + T_1$, is imposed on a 50 km wide domain centred at $x = 0$ km. This setting simulates a plume ascending from the transition zone (Fig. 1c).

We assume that both the lithospheric plate and the convecting mantle have a Newtonian rheology following an Arrhenius law:

$$\mu = \mu \exp\left(\frac{E_a + V_a \rho g Y}{RT}\right), \quad (4)$$

where μ_0 is a reference viscosity, $E_{\rm a}$ is the activation energy, $V_{\rm a}$ is the activation volume, g is the gravity acceleration, R is the gas constant, T is the temperature and Y is the depth. An upper and a lower viscosity cut-offs at 10^{16} and 10^{24} Pa s are imposed.

The density ρ varies following the state equation:

$$\rho = \rho_0 (1 - \alpha (T - T_r))(1 + \beta (P - P_r)), \quad (5)$$

where ρ_0 is the reference density at surface temperature $T_{\rm r}$ of 298.15 K and pressure $P_{\rm r}$ of 10^5 Pa, α is the coefficient of thermal expansion, β is the compressibility and P is the pressure. All constant parameters used in the models are listed in Table 1.

The box is discretized into 427 × 96 nodes. The mesh is refined vertically between 0 and 250 km depth and horizontally between −130 and 130 km, where the plume is introduced. The finest mesh is 5 km × 5 km and the largest 10 km × 10 km (Fig. 1a). The 1 942 560 initial markers are used, with a minimum of 16 markers in the smallest mesh. Resolution tests were performed by (1) further refining the grid (3 × 6 km), (2) doubling the number of markers and (3) reducing the maximum allowed marker displacement. Variations in temperature and velocity are always lower than 5 per cent (Appendix B). We also verified that the height of the vertically refined domain does not affect the thickness of the plume

Table 1. Constant parameters.

Symbol	Meaning	Value	Unit
H	Box high	700	Km
L	Box width	4000	Km
T_0	Top temperature	273	K
T_1	Bottom temperature	1623	K
μ_0	Reference viscosity	6.2–9.3–12.4	Pa s × 10^{10}
$E_{\rm a}$	Activation energy	2.5 × 10^5	J mol^{-1}
$V_{\rm a}$	Activation volume	0.25	J bar^{-1} mol^{-1}
G	Gravity	10	m s^{-2}
R	Gas constant	8.314	K^{-1} mol^{-1}
ρ_0	Reference density	3300	Kg m^{-3}
α	Thermal expansion	3 × 10^{-5}	K^{-1}
β	Compressibility	7.75 × 10^{-4}	kbar^{-1}
κ	Thermal diffusivity	7.75 × 10^{-7}	m^2 s^{-1}
Cp	Heat capacity	1250	J Kg^{-1} K^{-1}
K	Thermal conductivity	3.2	W m^{-1} K^{-1}

pancake and the maximum penetration depth in the asthenosphere of the cold lithospheric instabilities (Appendix B).

3 MODEL RESULTS

A total of 36 simulations have been performed to study the interactions between a rising plume and the overlying lithosphere (Fig. 2). Plate velocities, $V_{\rm plate}$, vary from 5 to 12.5 cm yr^{-1}; they may be represented by the dimensionless plate Peclet number, $Pe_{\rm plate}$, defined as $(V_{\rm plate}{\cdot}H)/\kappa$, where $H = 700$ km is the box height and κ is the thermal diffusivity. Three different mantle background viscosities, μ_1, defined at the bottom of the box ($H = 700$ km), were tested: 5×10^{20}, 7.5×10^{20} and 10^{21} Pa s. At sublithospheric depths (120 km), in the absence of a plume, viscosities are encompassed between 1.56×10^{19} and 3.24×10^{19} Pa s. For the model performed with the lowest viscosity at the base of the lithosphere (1.56×10^{19} Pa s) and a plate velocity, $V_{\rm plate}$, of 5 cm yr^{-1}, SSC initiates at lithosphere age of ∼60 Myr, as observed in previous works (van Hunen *et al.* 2005; Afonso *et al.* 2008; Zlotnik *et al.* 2008). SSC involves only the bottom, less viscous, part of the lithosphere. Theoretical, experimental and numerical studies (Morris & Canright 1984; Davaille & Jaupart 1993; Solomatov & Moresi 2000; Manga *et al.* 2001) showed that this sublayer encompasses fluid with temperatures ranging between the asthenosphere temperature $T_{\rm m}$ (here 1573 K) and $T_{\rm m} - \Delta T_{\rm e}$, where $\Delta T_{\rm e}$ is a characteristic temperature scale depending on the rheology through:

$$\Delta T_e\,(T_m) = -2.24\,\frac{\mu\,(T_m)}{\frac{\partial \mu}{\partial T}\,(T_m)} = -2.24\,\frac{R\,T_m^2}{E_a + V_a g \rho Y}. \qquad (6)$$

For our simulations, this means that only the bottom 250 K of the lithosphere will be fluid enough to get mobilized by SSC.

Anyway, in all the models discussed here, SSC does not affect yet the area where the plume impinges the lithosphere (around 40 Myr). Moreover, we verified in other runs that any pre-existing SSC is overcome by the one generated in the plume pancake.

The thermal anomaly, $\Delta T_{\rm plume}$, imposed to generate the plume ranges from 150 to 350 K. This thermal anomaly entails, when the plume impinges the base of the lithosphere, a sublithospheric viscosity ranging from 7.1×10^{17} Pa s at 115 km depth in simulation 23 to 4.56×10^{18} Pa s at 140 km depth in simulation 12 (Table 3).

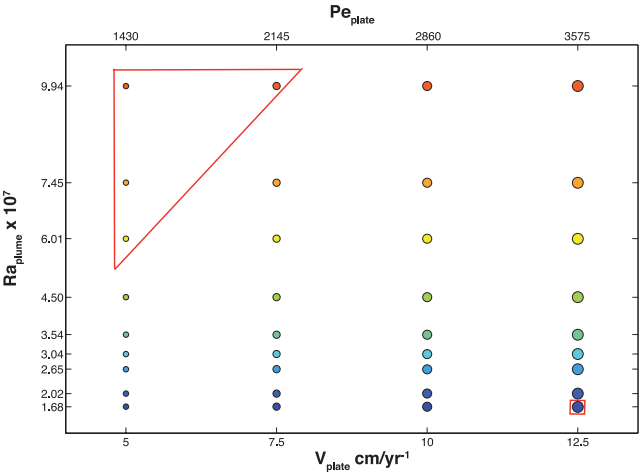

Figure 2. Plume Rayleigh numbers and plate velocities investigated in this paper. $Ra_{\rm plume}$ and plate velocity scales are indicated by the colour and sizes of the symbol sizes, which are the same in all figures of this paper. Simulations enclosed by the red lines do not reach a statistical plume–lithosphere equilibrium.

All simulations (Fig. 2) may be characterized by a combination of a $Pe_{\rm plate}$ and a plume Rayleigh number, $Ra_{\rm plume}$, defined as

$$Ra_{\rm plume} = \left(\alpha \rho g \left(T_{\rm plume} - T_0\right) H^3\right) \big/ \left(\mu_{\rm plume} \kappa\right), \qquad (7)$$

where α is the thermal expansion coefficient, $\mu_{\rm plume}$ is the viscosity of the plume material at 700 km depth, which depends on the background viscosity μ_1 and on the plume temperature $T_{\rm plume}$. $Ra_{\rm plume}$ is bracketed between 9.98×10^6 and 6.2×10^7 (Table 2 and Fig. 2).

3.1 Time–space evolution of the plume–lithosphere interaction

The sublithospheric layer undergoes a series of processes during the plume rise and its ensuing interaction with the overlying lithosphere. This evolution may be compartmented in three main stages (Fig. 3): (1) an early stage during which the plume rises up through the mantle (stage I, Fig. 3c), its dynamics being solely controlled by $Ra_{\rm plume}$, (2) a transient stage (stage II) when the plume head spreads out along the base of the lithosphere and (3) the final stage, which corresponds to the statistical thermomechanical equilibrium between the lithosphere and the underlying asthenosphere fed by hot plume material (stage III). This stage is characterized by the development of a SSC in the plume-fed sublithospheric layer. This statistical equilibrium is lost for times >35 Myr for strong plumes and for time >70 Myr for weak plumes (stage IV), probably due to interactions between the plume material and the external right-lateral no slip boundary, which slow down the downstream flow in the plume-fed sublithospheric layer. Results for stage IV are not considered in what follows.

The evolution of the system in time and space is clearly illustrated by space–time plots of the temperature (Fig. 3a) and the vertical velocity at sublithospheric depths. The depth at which these plots are computed is defined as a function of the interaction between the rising plume and the lithosphere; it corresponds to the depth where the vertical strain rate $(\partial V_{\rm y}/\partial y)$ in the plume conduit equals 20 per cent of the maximum vertical strain rate in the model, $(\partial V_{\rm y}/\partial y)_{\rm max}$. It ranges from 87 to 102 km, with no straightforward correlation with plate velocity. Fig. 3(a) depicts such a space–time diagram of the temperature in the sublithospheric layer, at a depth of 90.5 km (dashed black line in Fig. 3e), for a model with a plume thermal anomaly, $\Delta T_{\rm plume}$, of 200 K, impinging a 10 cm yr^{-1} velocity moving plate, in a mantle with a viscosity μ_1 of 5×10^{20} Pa s (simulation 7). The plume location and the onset of sublithospheric convective instabilities are characterized by steep spatial gradients of temperature. These plots clearly highlight the temporal and spatial periodicity of sublithospheric convective instabilities.

3.2 Plume rise and spreading at the base of the lithosphere (transition from stage I to stage II)

The initial impact of the plume on the base of the lithosphere results in the vertical displacement of the base of lithosphere. However, this displacement is limited since the hot plume can only pushes away the weakest part of the lithosphere, that is, the material within at most 250 K from the asthenosphere (cf. section 3; Olson *et al.* 1988; Androvandi *et al.* 2011). Indeed, we observe (Figs 3c and d) an uplift of the 1573 K isotherm, hereafter defined as the base of the lithosphere (initially at 90 km depth), by up to 15 km, but it does not significantly affect the 1473 K isotherm. The amplitude of

Table 2. Simulations list and corresponding dimensionless parameters.

Simulation	μ_1 (Pa s)	V_{plate} (cm yr^{-1})	Pe_{plate}	ΔT_{plume} (K)	μ_{plume} (Pa s)	Ra_{plume}
1	5×10^{20}	5	1430	150	3.90×10^{19}	1.69×10^{7}
2	5×10^{20}	7.5	2145	150	3.90×10^{19}	1.68×10^{7}
3	5×10^{20}	10	2859	150	3.91×10^{19}	1.68×10^{7}
4	5×10^{20}	12.5	3574	150	3.91×10^{19}	1.68×10^{7}
5	5×10^{20}	5	1430	200	2.23×10^{19}	3.04×10^{7}
6	5×10^{20}	7.5	2145	200	2.23×10^{19}	3.04×10^{7}
7	5×10^{20}	10	2859	200	2.23×10^{19}	3.04×10^{7}
8	5×10^{20}	12.5	3574	200	2.23×10^{19}	3.04×10^{7}
9	7.5×10^{20}	5	1430	200	3.36×10^{19}	2.02×10^{7}
10	7.5×10^{20}	7.5	2145	200	3.36×10^{19}	2.02×10^{7}
11	7.5×10^{20}	10	2859	200	3.36×10^{19}	2.02×10^{7}
12	7.5×10^{20}	12.5	3574	200	3.36×10^{19}	2.02×10^{7}
13	7.5×10^{20}	5	1430	250	1.98×10^{19}	3.54×10^{7}
14	7.5×10^{20}	7.5	2145	250	1.98×10^{19}	3.54×10^{7}
15	7.5×10^{20}	10	2859	250	1.98×10^{19}	3.54×10^{7}
16	7.5×10^{20}	12.5	3574	250	1.98×10^{19}	3.54×10^{7}
17	7.5×10^{20}	5	1430	300	1.20×10^{19}	6.01×10^{7}
18	7.5×10^{20}	7.5	2145	300	1.20×10^{19}	6.01×10^{7}
19	7.5×10^{20}	10	2859	300	1.20×10^{19}	6.01×10^{7}
20	7.5×10^{20}	12.5	3574	300	1.20×10^{19}	6.01×10^{7}
21	7.5×10^{20}	5	1430	350	7.49×10^{18}	9.94×10^{7}
22	7.5×10^{20}	7.5	2145	350	7.49×10^{18}	9.94×10^{7}
23	7.5×10^{20}	10	2859	350	7.49×10^{18}	9.94×10^{7}
24	7.5×10^{20}	12.5	3574	350	7.49×10^{18}	9.94×10^{7}
25	10×10^{20}	5	1430	250	2.64×10^{19}	2.65×10^{7}
26	10×10^{20}	7.5	2145	250	2.65×10^{19}	2.65×10^{7}
27	10×10^{20}	10	2859	250	2.65×10^{19}	2.65×10^{7}
28	10×10^{20}	12.5	3574	250	2.65×10^{19}	2.65×10^{7}
29	10×10^{20}	5	1430	300	1.60×10^{19}	4.50×10^{7}
30	10×10^{20}	7.5	2145	300	1.60×10^{19}	4.50×10^{7}
31	10×10^{20}	10	2859	300	1.60×10^{19}	4.50×10^{7}
32	10×10^{20}	12.5	3574	300	1.60×10^{19}	4.50×10^{7}
33	10×10^{20}	5	1430	350	9.99×10^{18}	7.45×10^{7}
34	10×10^{20}	7.5	2145	350	9.99×10^{18}	7.45×10^{7}
35	10×10^{20}	10	2859	350	9.99×10^{18}	7.45×10^{7}
36	10×10^{20}	12.5	3574	350	9.99×10^{18}	7.45×10^{7}

the 1573 K isotherm uplift depends on the plume ascent velocity, which is controlled by the plume buoyancy and the background mantle viscosity. This vertical displacement of the 1573 K isotherm is the only modification of the structure of the sublithospheric layer in this initial stage (Fig. 3b, stage I).

3.3 Conductive re-equilibration of the base of the lithosphere (stage II)

The initial mechanical uplift of the LAB is followed by a progressive deepening of the 1573 K isotherm, as a new thermal equilibrium is sought through conductive heat exchange at the base of the lithosphere. This stage II (Figs 3b and d) lasts between 3 Myr for strong plumes and 10 Myr for more sluggish plumes. It is ended by the onset of SSC. The first gravitational instability develops at the base of the lithosphere strongly downstream from the plume impact point. The next generation of instabilities forms closer to the plume conduit (Fig. 3a); this evolution continues until a stable location is reached (stage III).

3.4 Stable SSC in the plume-fed sublithospheric layer (stage III)

We consider that thermomechanical equilibrium between the moving lithosphere and the underneath plume material-fed sublithospheric layer is reached when the first convective drip forms at a steady distance from the plume axis (Figs 3a and b, stage III). This quasi-equilibrium state is defined as the time window where the lithospheric vertical heat flux, computed using the 1473 K and T_0 isotherms, is statistically constant over the last 500 km of the box right side. It is attained between 25 Myr (simulation 24) and 60 Myr (simulation 9) after the introduction of the plume in the model. The quasi-equilibrium state is lost when the plume conduit is significantly deflected due to interactions with the semi-natural condition on the right-lateral boundary (Fig. 3f, stage IV).

Five models do not reach thermomechanical equilibrium between the moving lithosphere and the underneath plume material-fed sublithospheric layer (simulations 4, 17, 21, 22 and 33 highlighted in Fig. 2). The first four simulations (17, 21, 22 and 33) are characterized by high plume ascending velocities and low plate velocities (ascending velocities at 600 km depth are ∼30–50 cm yr^{-1}). They have a well-developed SSC, but boundary effects are observed before equilibrium is reached. In contrast, in simulation 4, the plume ascending velocity (10.9 cm yr^{-1}) is lower than the plate motion (Vplate = 12.5 cm yr^{-1}). Hence, the plume is sheared by the plate-induced flow. Its impact under the lithosphere is not so well defined anymore, the plume conduit is strongly deflected and the whole interaction between the plume and the lithosphere is quite unstable.

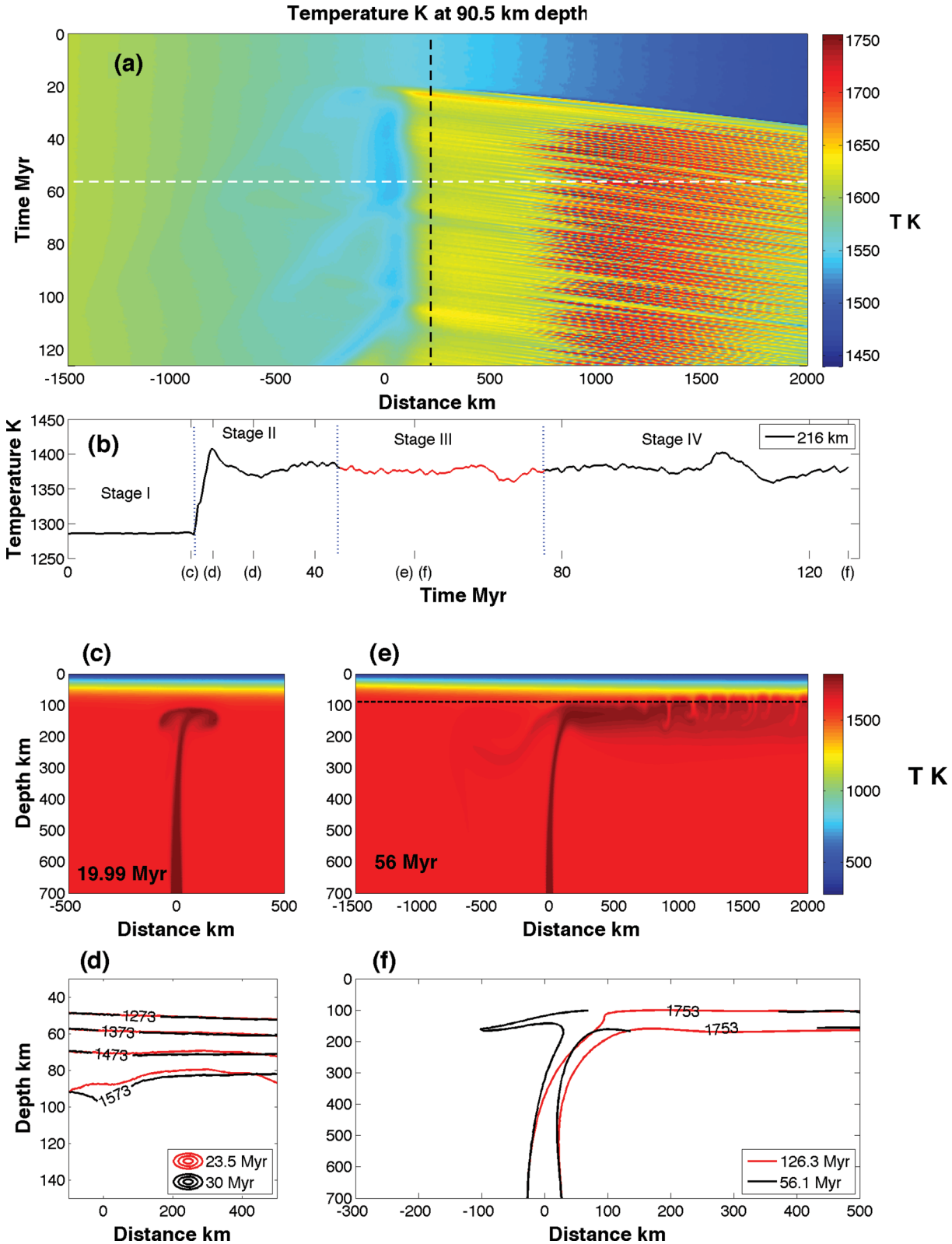

Figure 3. (a) Time–space plot of temperature computed at a depth of 90.5 km (dashed black line in the (e)). (b) Evolution in time of the temperature in the sublithospheric layer at 200 km ($x = 216$ km) downstream of the plume impact point (dashed black line in panel (a)). The different stages of the plume rise and interactions with the lithosphere are depicted. The location in time from (c) to (f) are labelled on the time axis. The thick red line corresponds to the time window associated with the statistical thermal equilibrium state. (c) Zoom on the plume rising in stage I; (d) conductive re-equilibrium at the base of the lithosphere (stage II); (e) showing the corresponding model characterized by a plume with a temperature anomaly ΔT_{plume} of 200 K impinging a plate moving at 10 cm yr^{-1} (simulation 7) 56 Myr after t_{init}, marked by a horizontal white dashed line in the time–space plot (a). (f) Influence of the open boundary effect on the plume conduit geometry (stage IV).

Table 3. Plume velocities, impact and onset locations, thickness of the plume puddle, temperature and viscosity.

Simulation	V_{plume} cm yr^{-1}	V_{up} cm yr^{-1}	V_{down} cm yr^{-1}	X_{impact} km	X_{onset} km	δ_{local} km	T_{local} K	μ_{local} Pa s
1	11.25	−4.12	6.16	53.9	566.4	43.46	1743	3.87×10^{18}
2	10.84	−3.5	7.57	84.7	737.6	44.84	1740	4.14×10^{18}
3	10.9	−3.1	9.11	83.4	838.0	44.87	1737	4.31×10^{18}
4	10.87	−1.22	10.98	126.1				
5	18.15	−7.55	6.93	11.7	306.5	38.77	1802	2.02×10^{18}
6	18.05	−5.78	9.17	59.1	504.4	43.22	1802	2.13×10^{18}
7	17.31	−4.58	9.6	107.6	616.6	45.11	1799	2.26×10^{18}
8	17.08	−4.39	10.67	98.2	700.5	43.64	1796	2.32×10^{18}
9	11.73	−3.78	5.53	53.3	500.3	44.58	1786	3.77×10^{18}
10	11.36	−2.87	6.98	104.8	748.4	47.31	1780	4.17×10^{18}
11	11.4	−2.62	8.55	96.6	804.5	46.57	1778	4.32×10^{18}
12	11.46	−1.65	10.48	119.8	841.7	49.01	1775	4.56×10^{18}
13	18.95	−7.1	6.82	6.9	255.3	38.95	1848	1.96×10^{18}
14	18.54	−4.9	8.06	69.0	482.7	44.79	1848	2.10×10^{18}
15	18.14	−3.72	9.15	116.7	627.1	46.73	1844	2.24×10^{18}
16	17.92	−3.48	10.58	114.8	714.4	45.92	1841	2.32×10^{18}
17	30.94	−13.63	10	−10.2				
18	29.9	−9.34	9.74	23.7	268.1	40.31	1910	1.15×10^{18}
19	29.8	−7.72	11.97	53.7	379.7	43.94	1910	1.20×10^{18}
20	29.7	−5.48	13.79	92.2	503.8	47.38	1908	1.26×10^{18}
21	49.28	−23.01	10.59	−23.9				
22	48.84	−17.77	15.45	−2.0				
23	48.15	−14.54	15.62	15.3	221.0	39.24	1967	7.10×10^{18}
24	48.06	−13.59	18.07	29.5	271.0	41.85	1967	7.30×10^{18}
25	13.9	−4.34	5.79	39.0	447.6	44.38	1835	3.12×10^{18}
26	13.75	−2.78	7.68	100.5	696.1	48.84	1831	3.44×10^{18}
27	13.38	−2.53	8.62	111.2	770.6	47.94	1826	3.62×10^{18}
28	13.39	−1.89	10.19	117.3	859.1	48.57	1822	3.82×10^{18}
29	22.41	−8.56	7.09	−7.4	234.3	38.97	1896	1.70×10^{18}
30	21.94	−5.59	8.43	56.6	401.4	44.69	1900	1.74×10^{18}
31	21.91	−3.71	10.52	104.0	581.8	48.68	1892	1.96×10^{18}
32	21.6	−3.21	12.2	126.6	678.8	48.56	1884	2.15×10^{18}
33	36.4	−15.46	9.52	−17.2				
34	35.64	−10.76	11.23	11.0	236.9	39.95	1961	9.91×10^{17}
35	35.5	−9.26	12.09	25.0	326.9	44.13	1961	1.04×10^{18}
36	35.32	−7.65	15.44	59.9	409.8	46.45	1961	1.07×10^{18}

3.5 Kinematics of the plume spreading at the base of the lithosphere

The plume rises vertically through the mantle with a dimensionless velocity Pe_{plume}, averaged over the equilibrium time window (deviations from the average $\leq$3 per cent), which increases linearly with Ra_{plume} (see Section 3.2). The large-scale flow associated with the plate motion starts to affect the plume dynamics at a depth of ∼300 km. At the base of the lithosphere, the plume material is either totally dragged by the plate (downstream flow) or spreads in two opposite directions, part of it flowing upstream, towards the ridge. The partition between the two flows depends on the ratio between the plume upwelling and the plate velocities (Sleep 1987).

The plume kinematics may be described by three velocities: the plume rise velocity, V_{plume}, defined as the maximum vertical velocity in the plume conduit estimated at a depth of 600 km in order to avoid any boundary effect from the open bottom of the model, the average (on a 150 km wide interval from the impact point, X_{impact}, see Section 4 for definition) upstream (opposite to the plate motion) and downstream (in the plate motion direction) horizontal velocities in the plume-filled sublithospheric layer, labelled V_{up} and V_{down}, respectively (Pe_{up} and Pe_{down}, respectively, in dimensionless form using the box height, H, and the thermal diffusivity, κ). These velocities are listed in Table 3. A plume rising beneath a stationary plate should spread symmetrically, that is, Pe_{down}/Pe_{up} should be equal to 1 for a flat LAB. In the present case, the weak inclination of the LAB towards the ridge slightly favours the upstream flow component. Drag by the moving plate, on the other hand, preferentially increases the downstream flow.

The plume dynamics at asthenospheric depths may therefore be characterized by two velocity ratios. The ratio between the up- and down-stream horizontal velocities of the plume material in the sublithospheric layer, Pe_{up}/Pe_{down}, depends on the ratio between plume upwelling and plate velocities, Pe_{plume}/Pe_{plate} (Fig. 4). For low Pe_{plume}/Pe_{plate} ratios, the plate motion drags most plume material and the downstream flow is dominant (Fig. 4a). As Pe_{plume}/Pe_{plate} increases, an increasing part of the plume material flows upstream, towards the ridge (Fig. 4b). These results are consistent with the regime diagram relating the plume–lithosphere interaction to plume buoyancy and background mantle viscosity for a constant plate velocity derived by Thoraval *et al.* (2006), which distinguishes between low buoyancy plumes deflected or entrained downstream by large-scale flow induced by the plate motion and high buoyancy

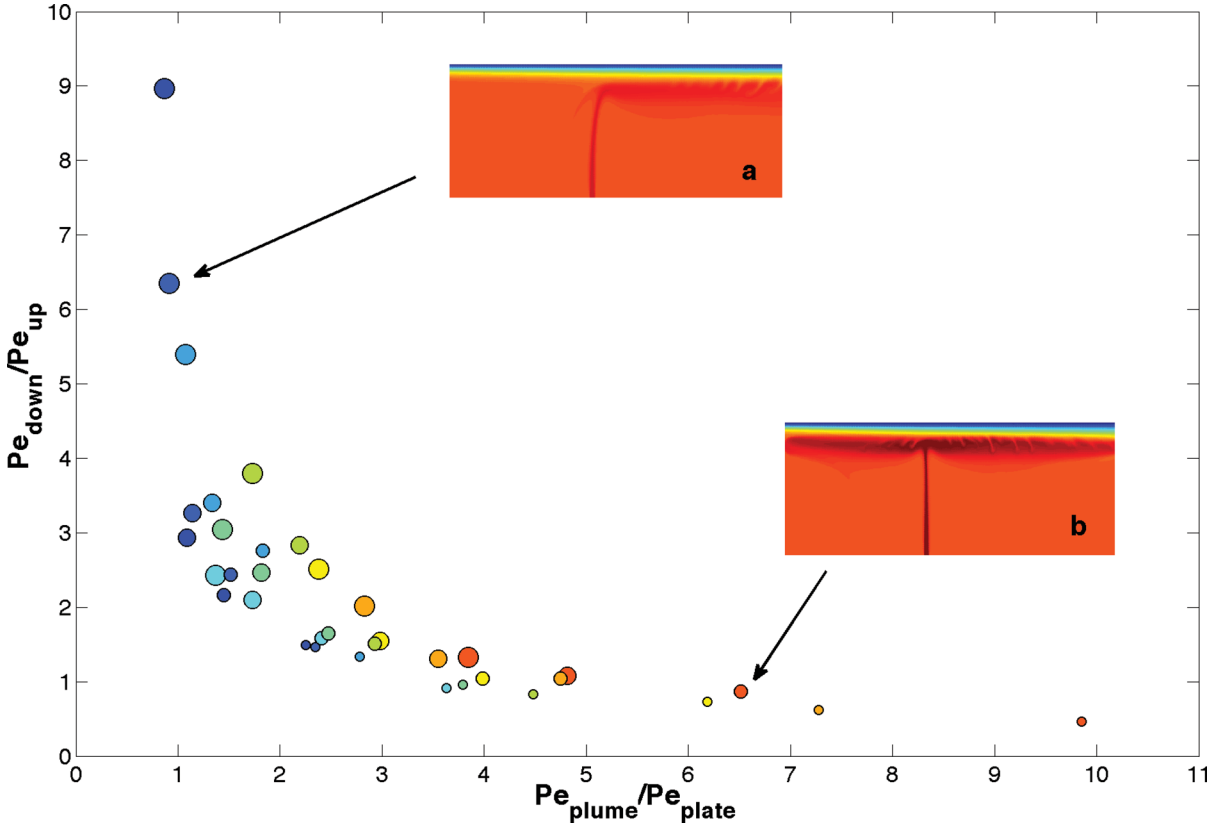

Figure 4. Plume spreading as a function of the plate and plume dimensionless velocities. Inserts show examples of end-member cases: (a) for low Ra_{plume} and high Pe_{plume}, plate motion drags most plume material dominant downstream flow (simulation 12). (b) High Ra_{plume} yields a strong upstream flow (simulation 22). Increasing Ra_{plume} and plate velocity scales are indicated by hotter colours and larger sizes of the symbols, cf. Fig. 2.

plumes overrunning the plate-induced flow. However, one should note that both regime diagrams were derived based on 2-D models. Three-dimensional models show that the plume material spreads out not only parallel to the plate motion but also laterally, forming a parabolic shape elongated in the direction of plate motion (Ribe & Christensen 1994; Moore *et al.* 1998). This lateral spreading largely reduces the upstream flow.

4 DYNAMICS OF SMALL-SCALE CONVECTION IN THE PLUME-FED SUBLITHOSPHERIC LAYER

4.1 Convective regime in the hot sublayer

To evaluate the convective regime in the hot plume puddle under the lithosphere, we can estimate its Rayleigh number, Ra_{sub}, based on the thickness and properties of the layer encompassed between the maximum temperature, T_{local}, in the plume pancake and the temperature at the base of the lithosphere (LAB), defined here as $T_{LAB} = 1573$ K. T_{local} and the corresponding viscosity, $\mu_{local} = \mu(T_{local})$, in the sublithospheric layer are averaged horizontally between the plume impact point and the onset location (Figs 5c and d). This local Rayleigh number thus writes as

$$Ra_{sub} = \frac{\alpha\rho g\,(T_{local} - T_{LAB})\delta^3_{local}}{\kappa\mu_{local}}, \tag{8}$$

where $\delta_{local} = (Y_{local} - Y_{LAB})$ is the characteristic thickness of the plume puddle, and Y_{LAB} and Y_{local} are the depths of the isotherms T_{local} and T_{LAB}, respectively. These parameters are listed in Table 3.

We see that for all experiments, Ra_{sub} is over 4000, that is, greater than the critical Ra for convection to occur (∼1100 for our case, Chandrasekhar 1961).

4.2 Onset of convection in the hot plume sublayer

SSC beneath a rigid lid cooling from above has extensively been studied through numerical and laboratory models using various temperature- and pressure-dependent rheologies and heating modes (from below or within) (Davaille & Jaupart 1993, 1994; Choblet & Sotin 2000; Korenaga & Jordan 2002, 2003; Huang *et al.* 2003; Van Hunen *et al.* 2003; Dumoulin *et al.* 2005). These studies derived scaling laws relating the onset time, t_c, of SSC to the Rayleigh number of the mantle and to the rheology, in particular through the dimensionless temperature scale $\theta(T_m) = (T_m - T_o)/\Delta T_e(T_m)$:

$$\frac{t_c}{H^2/\kappa} = C \cdot Ra^{-2/3}\theta^{\beta}, \tag{9}$$

where C is an experimental constant and Ra is defined as

$$Ra\,(T_m) = \frac{\alpha\rho g\,(T_m - T_0)H^3}{\kappa\mu\,(T_m)}. \tag{10}$$

The exponent β was found to vary, depending on the θ range considered, from 4/3 (Davaille & Jaupart 1993; Choblet & Sotin 2000) to ∼0.7 (Korenaga & Jordan 2002, 2003; Huang *et al.* 2003; Van Hunen *et al.* 2003). The latter value corresponds to the mantle θ-range (∼5–20). The −2/3 Ra-exponent reveals that the SSC phenomenon is truly a boundary layer process, as its onset does not depend on the total depth of the mantle layer considered.

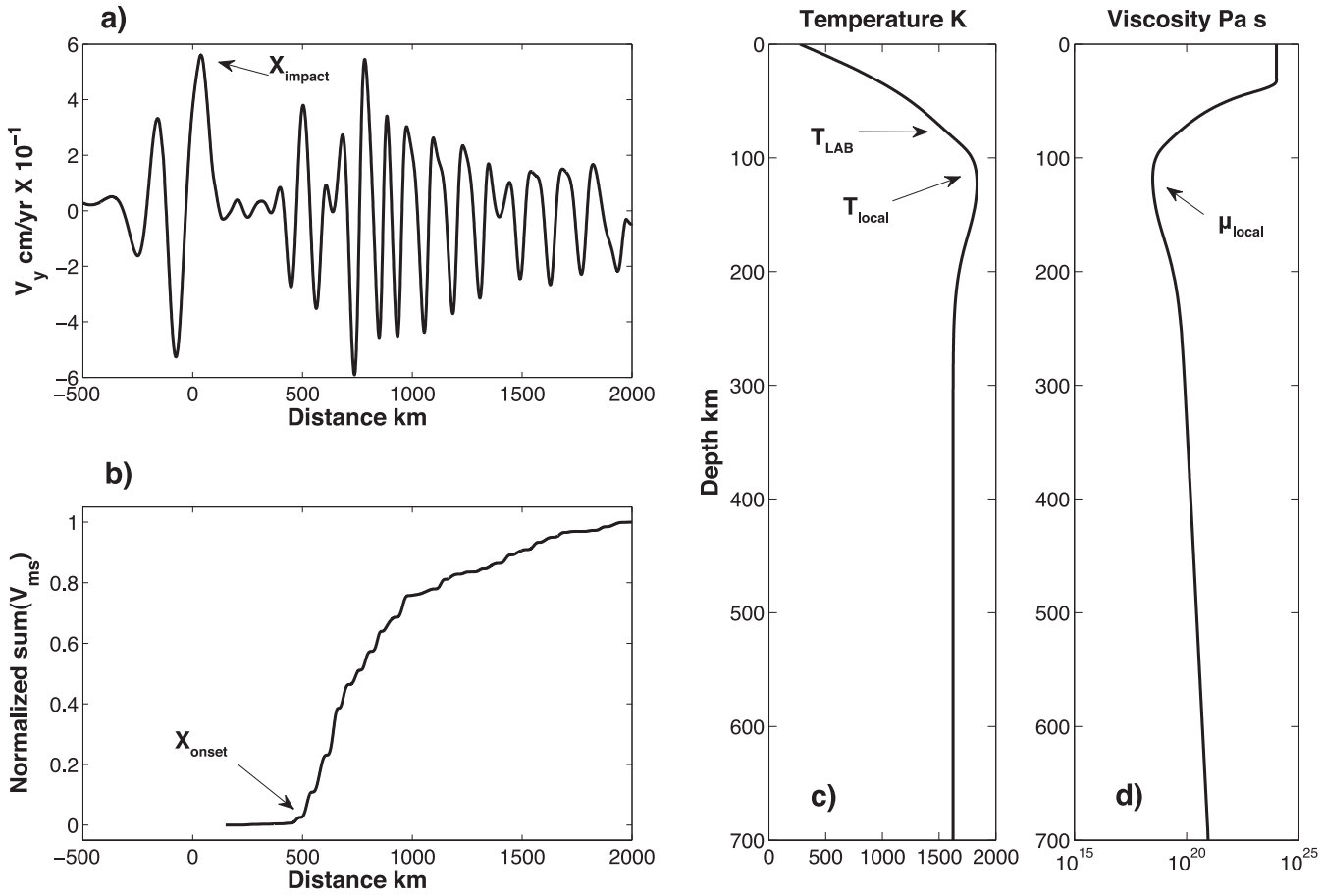

Figure 5. Definition of the impact point (X_{impact}) of the SSC onset location (X_{onset}), as well as of the temperatures (T_{local} and T_{LAB}) and viscosity (μ_{local}) in the plume-fed sublithospheric layer. (a) Vertical velocity in the sublithospheric layer, the impact point is located at the maximum velocity. (b) Sum of the square of the vertical velocities in the sublithospheric layer normalized by the maximum values, the SSC onset is located at 1 per cent of the sum over the entire window. (c) and (d) Average temperature and viscosity profiles between X_{impact} and X_{onset}; arrows indicate the values used to define the Ra_{local}. The corresponding model characterized by a plume with a temperature anomaly ΔT_{plume} of 250 K impinging a plate moving at 5 cm yr^{-1} (simulation 25) 70.7 Myr after t_{init}.

The effect of the plate motion on the SSC beneath a cooling plate has been studied in both 2-D and 3-D. In 3-D, strong shearing due to plate motion favours the development of SSC convection rolls with an axis parallel to the plate motion (longitudinal rolls) relative to those with an axis perpendicular to the plate motion (transversal rolls) (Richter 1973; Houseman 1983). In the same type of 2-D geometry as we are studying here, only transversal rolls develop and an increase of the onset time is observed with increasing plate velocity (Huang *et al.* 2003; Van Hunen *et al.* 2003). In 3-D, the opposite trend is observed with a slight decrease of the onset time with increasing plate velocity (Van Hunen *et al.* 2003). Here, we analyse if similar relations exist for SSC in a plume-fed sublithospheric layer. We define the onset time of SSC, t_{c}, as the time for the first instability drip to develop once the plume has impacted the lithosphere.

The horizontal location of the plume impact point, X_{impact}, is defined as the location of the maximum vertical plume velocity, averaged over the equilibrium time window (Fig. 5a), in the time–space plots of vertical velocities at the base of the lithosphere. It corresponds to the location where the plume conduit impacts the lithosphere. In most cases, the plume head impinges the base of the lithosphere not exactly atop the plume axis, which corresponds to a 40 Myr old lithosphere ($x = 0$ km), but downstream from this point, due to a slight deflection of the plume conduit by the shearing induced by the plate motion. The impact point location varies from above the plume axis (simulations 17, 21, 22, 29 and 33) to up to 125 km (simulations 4 and 32) downstream from the initial plume conduit location (2000 km from the ridge).

The horizontal location of the first dripping instability, X_{onset}, is defined by a marked increase in vertical velocities in the plume-fed sublithospheric layer (Fig. 5a). It is defined as the location, averaged over the equilibrium time window, where the sum of the squared vertical velocities, calculated from the impact point to the right boundary of the model, equals 1 per cent of the sum over the entire interval (Fig. 5b):

$$\sum_{i=1}^{n} V_y^2\,(x\,(i)) = 0.01 \sum_{i=1}^{N} V_y^2\,(x\,(i)), \tag{11}$$

where N is the total number of points between the impact point to the right boundary of the model and n is the index of the position where the relationship is satisfied ($x(n) = X_{\text{onset}}$). X_{onset} ranges from 206 km (simulation 23) to 755 km (simulation 3) away from the impact point (X_{impact}).

The onset time of SSC is estimated with respect to the plume impact location, as our final goal is to look at the efficiency of lithosphere thinning induced by the plume heating to compare our modelling results to geophysical observations of lithosphere thermal structures. The onset time of SSC, t_{c}, is then defined as the difference between X_{onset} and X_{impact} converted in time by dividing by V_{plate}.

For all simulations, the impact points and SSC onset locations, as well as the SSC onset time, are given in Table 3.

4.3 Influence of the hot plume material on the onset of SSC

To keep in line with the previous studies, we study the variation of the onset time of SSC as a function of $Ra(T_{\rm local}) = Ra_{\rm SSC}$. This also allows to consider not only the material with temperature above $T_{\rm LAB}$ (as considering $Ra_{\rm sub}$ would do) but also the material belonging to the less viscous part of the lithosphere. For all our simulations, the parameter θ ranges between 12.2 and 15.2. In a first step, we therefore consider it to be constant. Fig. 6 shows the variation of $t_{\rm c}$ as a function of the Rayleigh number $Ra_{\rm SSC}$ and the plate speed. We also included six extra simulations with a thermal diffusivity of 10^{-6} m^2 s^{-1}, for lithosphere moving with two plate velocities (7.5 and 10 cm yr^{-1}) and two background mantle viscosities at 700 km depth (5×10^{20} and 7.5×10^{20} Pa s). As previously reported (e.g. Davaille & Jaupart 1994; Huang *et al.* 2003; Dumoulin *et al.* 2005), $t_{\rm c}$ decreases with increasing $Ra_{\rm SSC}$ and the fit on all the data points gives:

$$\frac{t_c}{H^2/\kappa} = 146.7\,(\pm 0.4)\,Ra_{SSC}^{-0.679\pm0.046}. \quad (12)$$

The Ra-exponent is very close to $-2/3$, showing again that the SSC process is local and does not depend on the mantle layer thickness. We also plotted in green the scaling obtained for SSC developing under a 2-D ageing lithosphere (Huang *et al.* 2003) or a 3-D moving lithosphere (Van Hunen *et al.* 2003) above a mantle at the same temperature $T_{\rm local}$ as in our plume, and for the same θ range:

$$\frac{t_c}{H^2/\kappa} = C \cdot Ra^{-0.68}\theta^{0.74}, \quad (13)$$

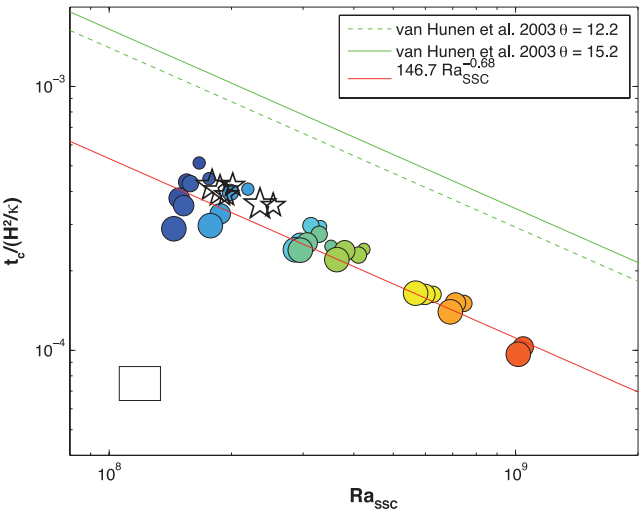

Figure 6. Onset dimensionless time of the SSC, $t_{\rm c}$, as a function of the Rayleigh number, $Ra_{\rm SSC}$. The red line is the scaling (12). The green lines are the scaling obtained for SSC developing under a 3-D moving lithosphere (Van Hunen *et al.* 2003) with the $Ra_{\rm SSC}$ as in our simulations and θ of 12.2 and 15.2 (dashed and solid line, respectively). Increasing $Ra_{\rm plume}$ and plate velocity scales are indicated by hotter colours and larger sizes of the symbols, cf. Fig. 2. The stars are the six extra simulations with a thermal diffusivity of 10^{-6} m^2 s^{-1}. The square in the bottom right is the uncertainty on $t_{\rm c}$.

where $C = 60.6$ is an experimental constant. This would correspond to the case where the plume is at the ridge and the lithosphere is growing above this abnormally hot mantle. Given the uncertainties on the data, we see that the scaling (13) would also explain well our data, albeit with a lower constant $C = 21.5 \pm 3.0$ (Fig. 8). This would tend to show that a same process, the gravitational instability of the bottom of the lithosphere, is responsible for SSC, whether it is under a normal lithosphere or under a plume. However, Fig. 6 also shows two important features: (i) SSC starts earlier under a mature lithosphere when a plume is involved and (ii) there is some systematic variation of the data as a function of the plate velocity for the lowest Rayleigh numbers.

4.3.1 *Earlier SSC onset*

The values of the constant C are significantly lower than the ones found for the onset of SSC under a lithosphere cooling above a hot mantle. SSC is starting much sooner in our case, because the plume hit an already grown lithosphere. Therefore, even though the 40-Myr-old lithosphere was not yet thick enough to present SSC in the parameter range that we studied, it was already much closer to instability than a lithosphere growing from the ridge. Moreover, the presence of the hot plume puddle is increasing the local Rayleigh number, therefore decreasing the time needed for the bottom of the lithosphere to become unstable: as already mentioned in Section 3.3, SSC starts within 2–10 Myr after plume impact, while it would have started at least 20 Myr later if there had been no plume.

4.3.2 *Influence of the plate velocity*

Fig. 6 shows that SSC onset time decreases with increasing plate velocities, especially for the lowest $Ra_{\rm plume}$. This contrasts with previous studies of onset of SSC beneath a cooling plate in 2-D, where high plate velocities delay the onset of SSC (Van Hunen *et al.* 2003; Zlotnik *et al.* 2008). Profiles of the horizontal velocity, $V_{\rm x}$, in the plume-fed asthenosphere (Fig. 7a) show that shearing between the lithosphere and the asthenosphere occurs for all plate velocities, albeit shear senses may change. For low $Ra_{\rm plume}$, shearing results mainly from plate drag (dominant Couette flow). This is a case comparable with the previous works (Van Hunen *et al.* 2003; Zlotnik *et al.* 2008). On the other hand, for high $Ra_{\rm plume}$, the plume spreads faster than the plate motion (dominant Poiseuille flow; Fig. 7b). Shearing in the sublithospheric layer cannot therefore explain the discrepancy between the present results and previous ones.

This discrepancy may, however, be explained by considering the influence of the thickness of the unstable sublayer at the base of the lithosphere on the SSC development. Two processes control the thickness of the lithosphere, and hence, of the unstable sublayer at its base before the triggering of SSC: the mechanical thinning of the bottom of the plate by the impacting plume, and the heating of the base of the lithosphere by the plume material. Both processes occur downstream of the impact, but also upstream. The latter is more efficient for slower plates that enhance the upstream flow (Fig. 4a), which, in turn, reduces the thickness of the lithospheric sublayer about to be affected by SSC, delaying its onset. This would explain why the SSC downstream of the plume impact point is triggered later for slow plate velocities and decreases with increasing plate velocities (Figs 6 and 8).

In case of vigorous plumes (high $Ra_{\rm plume}$), SSC can also occur in the sublithospheric layer heated by the upstream plume flow. The convective instabilities developing in this layer also induce

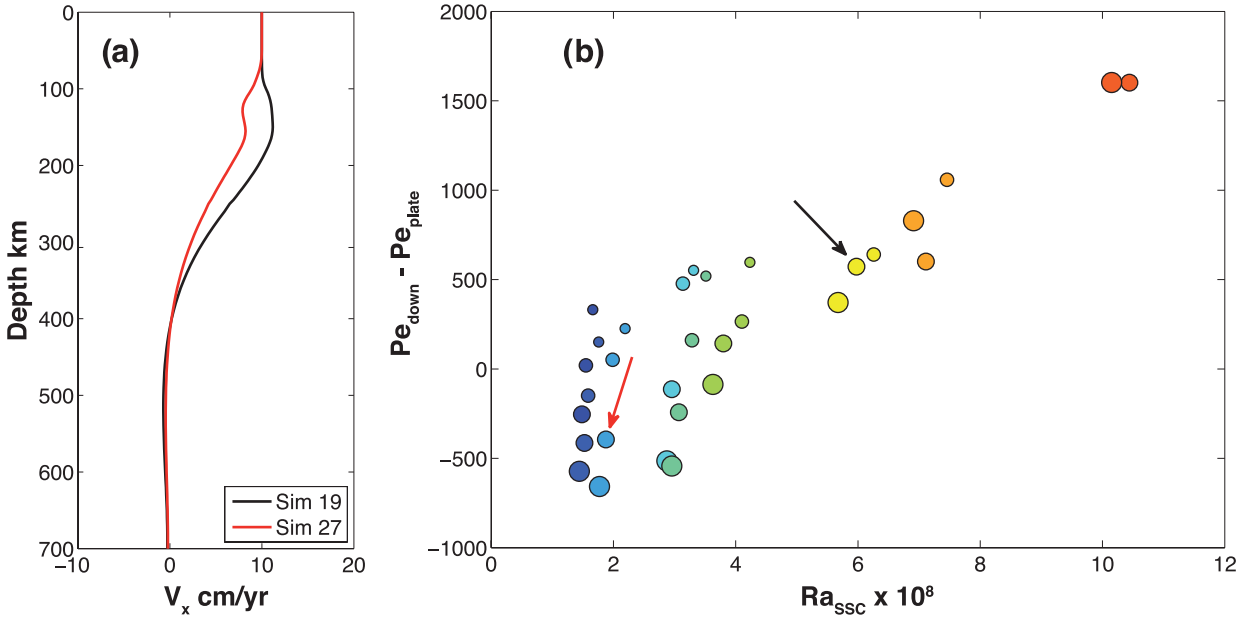

Figure 7. Shearing in the plume-fed sublithospheric layer. (a) Horizontal velocity profiles averaged on a 150 km wide interval from the impact point, X_{impact}, in simulations 19 and 27. (b) Difference in horizontal velocity between the asthenosphere and plate as function of Ra_{plume} and plate velocity (increasing symbol sizes indicate higher velocities). Fast rising plumes (high Ra_{plume}) result in a composite Couette and Poiseuille flow in the sublithospheric layer. The arrows indicate the models in (a). Increasing Ra_{plume} and plate velocity scales are indicated by hotter colours and larger sizes of the symbols, cf. Fig. 2.

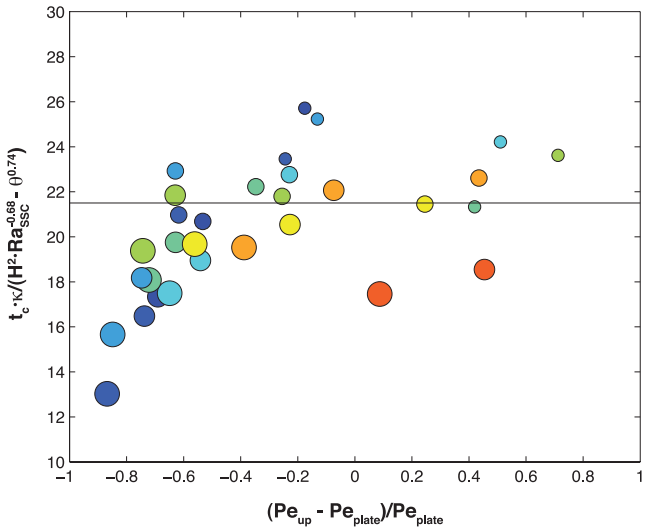

Figure 8. Variations of the data from the scaling law (13) obtained with a constant $C = 21.5$ (black line). SSC is starting sooner for weaker plumes and fast plate velocity. Increasing Ra_{plume} and plate velocity scales are indicated by hotter colours and larger sizes of the symbols, cf. Fig. 2.

thermomechanical erosion of the thermal boundary layer upstream of the impact point, and hence delay the onset of SSC in the downstream domain. However, the strong heating of the lithosphere base combined to the very low basal viscosity associated to high Ra_{plume} sustains the thinned sublithospheric layer close to instability at all times, promoting low SSC onset downstream almost independently of the plate velocity (Fig. 6).

5 LITHOSPHERE EROSION

The lithosphere erosion is estimated as the depth difference for a given isotherm between the equilibrium state without plume ($t = t_{\text{init}}$), and the new quasi-equilibrium state reached after the introduction of the plume. We discriminate between the different processes modifying the thermal structure of the lithosphere by considering thermal-mechanical erosion, on the one hand, which includes all modes of mechanical deformation of the LAB (notably SSC), and conductive heating, on the other hand. Four processes contribute to the vertical displacement of lithosphere isotherms: (1) a vertical displacement associated with the upstream flow of plume material. This process is most effective for slow plates and high Ra_{plume} (Fig. 4b); (2) a vertical displacement associated with the ascending flow in the plume conduit where it impinges on the base of the lithosphere, which only affects the LAB (1573 K isotherm); (3) a thermal conductive heating of the base of the lithosphere by the hotter than normal plume material that takes place from the plume impact point until SSC initiates downstream (at $x = X_{\text{onset}}$). Downstream, in the time interval between plume impact and SSC onset (t_c), heat is transferred across a distance of $\sqrt{\kappa t_c}$, which for the thermal diffusivity used in the present models is ca. 10 km. This is in agreement with the uplift of up to 10 km of the 1473 K isotherm relative to its initial position at the time t_{init} (Fig. 9b) modelled for fast plates and low Ra_{plume}, which show a weak upstream flow; (4) a thermomechanical erosion by SSC, which results in an enhanced heat flow at the base of the lithosphere.

Considering all the processes mentioned above, high plate velocities and low Ra_{plume} yield limited lithosphere erosion: only the isotherms 1473 and 1573 K are uplifted. In contrast, for slow plate velocities and high Ra_{plume}, even the 1073 K isotherm undergoes a small uplift (5 km relative to the initial equilibrium state before the introduction of the plume, Fig. 9a).

For slow plate velocities, isotherms are the shallowest close to the onset of SSC, because dripping of a cold instability results in a rapid cooling of the plume pancake (Fig. 9a). For fast plate velocities, isotherms are the shallowest within the domain affected by SSC at varying distance of the onset point (Fig. 9b). The maximum uplift of the isotherms 1373, 1473 and 1573 K is 5 km (simulation 29), 14 km (simulation 30) and 32 km (simulation 28), respectively. Due to the

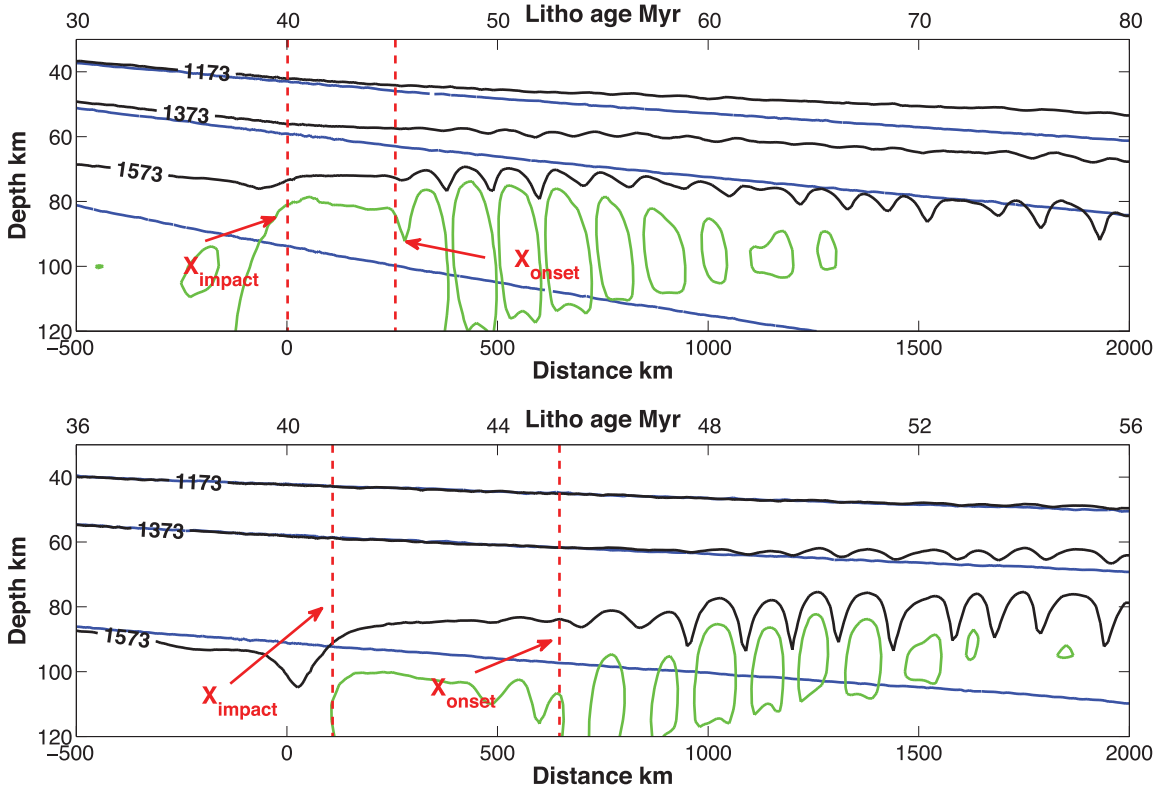

Figure 9. Lithosphere erosion characterized by the difference between the isotherms at time t_{init} (blue lines, equilibrium state before the introduction of the plume) and at the end of the simulation (black lines, showing the plume–lithosphere equilibrium state). Dashed red lines indicate the location of the impact point and the onset of SSC. Green contour indicates partial melting of 5 per cent. (a) For intermediate Raplume and low plate velocities (simulation 13), the minimum depth of the 1573 K isotherm is located close to Xonset; this thinning is followed by a slow thickening of the lithosphere due to cooling of the plume-fed sublithospheric layer. Note the upwelling of the 1573 K isotherm upstream of the impact point due to the strong upstream flow. (b) Higher plate velocities (simulation 16) delay erosion; the minimum depth of the 1573 K isotherm is observed far away from the X_{onset}.

low thermal diffusivity of upper mantle rocks at the temperatures prevailing at the base of the lithosphere ($6–10 \times 10^{-7}$ m^2 s^{-1}; Gibert *et al.* 2005; Tommasi *et al.* 2001), thermal re-equilibration of the entire lithosphere is never achieved.

An overview of the relationship between the lithosphere erosion, characterized by the minimum depth of the 1573 K isotherm, plate velocity and plume vigour are displayed in Fig. 10. Both parameters are positively correlated to the vertical displacement of the LAB, but Ra_{plume} has a stronger effect than the plate velocity. The 1573 K isotherm is the shallowest (72 km depth) for slow plates and vigorous plumes. Cold plumes impacting fast-moving plates result in almost no erosion of the lithosphere; the 1573 K isotherm is always deeper than 85 km. Except for plates moving at 5 cm yr^{-1}, which systematically show the shallowest isotherms at the onset of SSC, indicating that erosion is essentially produced by the upstream flow, ascending velocity in the plume conduit, and conductive heating. The maximum lithosphere erosion occurs within 5–10 Myr after the onset of SSC (that is, within 6–18 Myr from the plume impact). This delay is inversely proportional to Ra_{plume} (Fig. 10b).

In summary, our simulations suggest that SSC in the plume-fed sublithospheric layer may produce an uplift of the LAB equivalent to the values observed by seismic methods beneath Cape Verde (Lodge & Helffrich 2006). Moreover, we show that consistently with observations at Hawaii (Li *et al.* 2004) for a fast-moving plate, the minimum depth of the LAB should be observed downstream from the impact point. However, the extreme erosion of the lithosphere to depths <50 km observed beneath Oahu (Li *et al.* 2004) was never obtained in our simulations. A strong lithospheric erosion by SSC, as proposed by Li *et al.* (2004), downstream of the island of Hawaii could not be consistent with geological observations because it could produce massive decompression melting and volcanism (Ballmer *et al.* 2011). Moreover, the amplitude of erosion may even be weaker in 3-D, because it will be distributed over a larger area and, as discussed in Section 3.5, the upstream flow will be reduced.

On the other hand, considering the effects of partial melting and melt migration on mantle viscosity and density may allow for a more efficient erosion of the lithosphere than observed in the present simulations. Melt may reduce the viscosity by one order of magnitude even for low melt fractions (<1 per cent, Takei & Holtzman 2009). This viscosity reduction would allow for higher Ra_{SSC} and hence result in a more vigorous SSC in the sublithospheric layer. Furthermore, melt extraction decreases the density of the residual mantle (Jordan 1979; Schutt & Lesher 2006) increasing the density contrast with the underlying base of the lithosphere. On the other hand, partial melting may also limit lithospheric erosion through water depletion and subsequent strengthening of the solid residue (e.g. Karato 1986). For instance, if melting at the ridge results in development of a 60–70-km-thick dehydrated and hence stiff mantle layer (Hirth & Kohlstedt 1996); this may stabilize the lithosphere base, suppressing the development of SSC beneath young plates (Zaranek & Parmentier 2004; Afonso *et al.* 2008).

In the present models, partial melting has simply been predicted by determining the domains where *P-T* conditions exceed the anhydrous peridotite solidus (Katz *et al.* 2003). Partial melting always

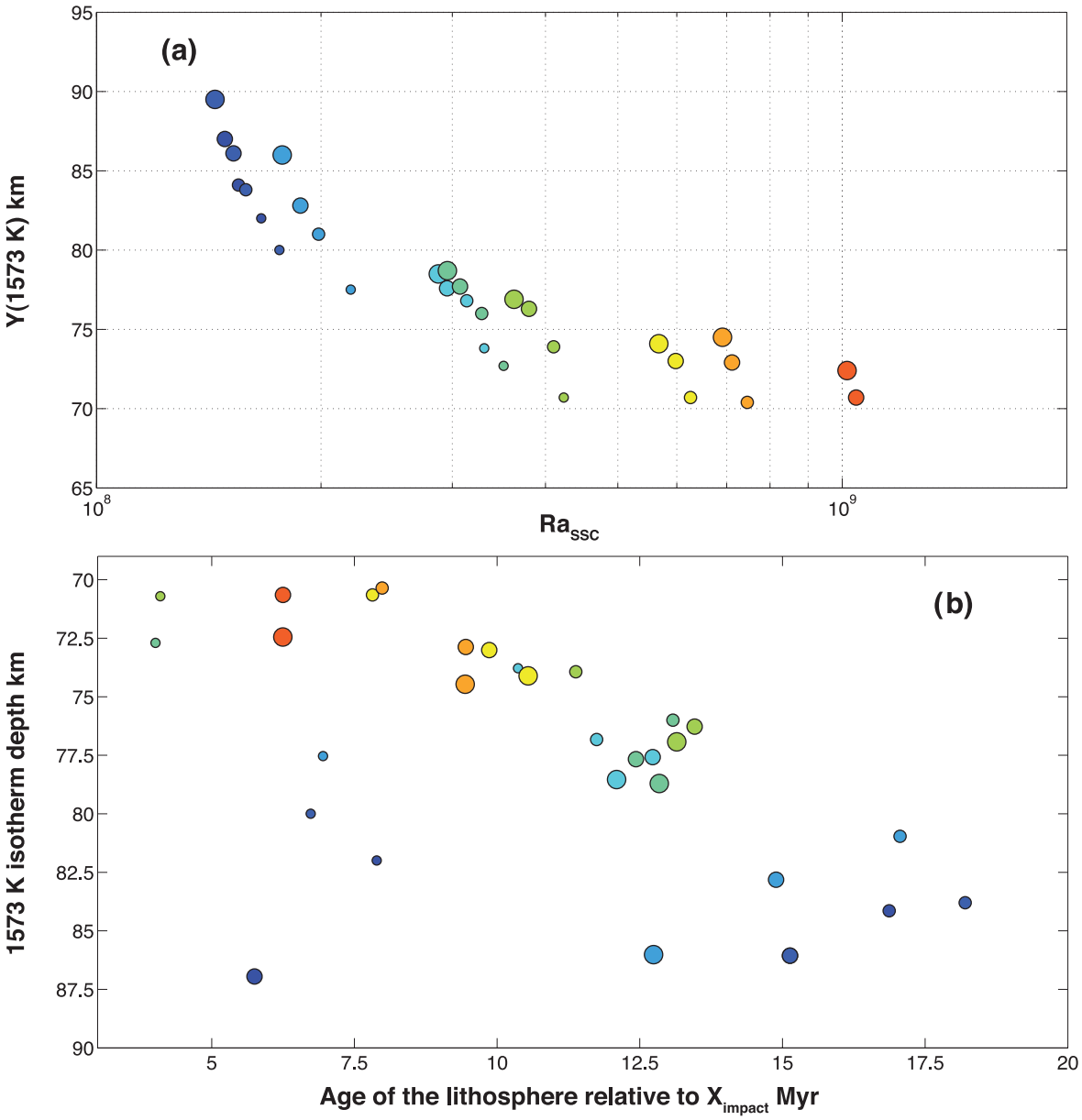

Figure 10. (a) Minimum depth of the LAB, characterized by the 1573 K isotherm. The shallowest LAB is observed when energetic plumes impact slow plates. (b) Distance (converted in time, Myr) between the plume impact and the location at which the minimum depth of the 1573 K isotherm is achieved. Increasing Ra_{plume} and plate velocity scales are indicated by hotter colours and larger sizes of the symbols, cf. Fig. 2.

occurs in the vicinity of the plume impact, but it may extend far away from it for plumes with high-temperature anomalies (Fig. 9), with further development of low amounts of partial melting at the base of the lithosphere destabilized by SSC, as predicted by Ballmer *et al.* (2011). A more accurate modelling of melt generation and its effects on the plume–lithosphere interactions will be presented in a companion article, currently in preparation.

6 CONCLUSION

Plume–lithosphere interactions were studied by 2-D numerical simulations using a thermomechanical numerical model based on a finite-difference method on a staggered grid and marker in cell method (Gerya & Yuen 2003). We focused on the kinematics of the plume as it impacts a moving plate, on the dynamics of time-dependent small-scale convective instabilities developing in the low-viscosity layer formed by spreading of hot plume material at the base of the lithosphere, and on its consequences for the thermal rejuvenation of the lithosphere.

The injection of hot plume material into the asthenosphere accelerates the onset of SSC downstream of the plume impact. This is due to the conjugate effect of mechanical erosion of the less viscous part of the lithosphere by the plume upstream and downstream flows, and the reheating of the lithosphere by the hot plume material. The onset time of SSC, t_c, depends primarily on the local Rayleigh number in the reheated asthenosphere, which, in turn, is closely related to the plume strength (characterized by Ra_{plume}). t_c decreases with increasing Ra_{plume}. A weaker and more complicated dependence on the plate velocity is observed. For vigorous, hot plumes (high Ra_{plume}) t_c does not depend on plate velocity; while for more sluggish plumes (low to intermediate Ra_{plume}), t_c also decreases with increasing plate velocity.

Four processes contribute to the erosion of the lithosphere, the signature of which is the vertical displacement of the isotherms: (1) a vertical displacement associated with the upstream flow; (2) a vertical displacement associated with the ascending flow in the plume conduit at the impact at the base of the lithosphere; (3) thermal conductive heating of the base of the lithosphere in response to the temperature increase in the plume-fed sublithospheric layer; (4) thermomechanical erosion by SSC, which results in an enhanced heat flow at the base of the lithosphere. Erosion increases with increasing Ra_{plume} and decreasing plate velocity. Minimum depths of the LAB (71 km for an 44 Myr old plate) are observed 205 km away from the plume impact for the highest Ra_{plume} and lowest plate velocities. Due to the low thermal diffusivity of upper mantle rocks at temperatures prevailing at the base of the lithosphere ($6–10 \times 10^{-7}$ m^2 s^{-1}; Tommasi *et al.* 2001; Gibert *et al.* 2005), thermal re-equilibration of the lithosphere is never achieved, but the impact of a plume results in a strong transient thermal gradient at the base of the lithosphere.

Despite the limited uplift of the LAB, which never exceeds 30 km in our models, SSC in the plume-fed sublithospheric layer appears as a plausible mechanism to explain the lithosphere erosion observed in seismic images atop hotspots in oceanic plates. Yet, to better simulate the plume lithosphere interaction and the ensuing ability of the plume to thin the lithosphere, additional developments are required to 1) study the influence of a 3-D geometry and 2) include the effects of partial melting and melt transport on mantle rheology and density.

ACKNOWLEDGEMENTS

This work benefited from discussions with C. Thoraval. We thank J. C. Afonso and M. Ballmer for their valuable suggestions. The research leading to these results has been funded by the Initial Training Network (ITN) Crystal2Plate, an FP7-funded Marie Curie Action under grant agreement number PITN-GA-2008-215353.

REFERENCES

Afonso, J.C., Zlotnik, S. & Fernàndez, M., 2008. The effects of compositional and rheological stratifications on small-scale convection under the oceans: implications for the thickness of oceanic lithosphere and seafloor flattening, *Geophys. Res. Lett.,* **35,** L20308, doi:10.1029/2008GL035419.

Androvandi, S., Davaille, A., Limare, A., Fouquier, A. & Marais, C., 2011. At least three scales of convection in a mantle with strongly temperature-dependent viscosity, *Phys. Earth planet. Inter.,* **188,** 132–141.

Ballmer, M.D., Ito, G., van Hunen, J. & Tackley, P.J., 2011. Spatial and temporal variability in Hawaiian hotspot volcanism induced by small-scale convection, *Nature Geosci.,* **4,** 457–460.

Ballmer, M.D., van Hunen, J., Ito, G., Bianco, T.A. & Tackley, P.J., 2009. Intraplate volcanism with complex age–distance patterns - a case for small-scale sublithospheric convection, *Geochem. Geophys. Geosyst.,* **10,** Q06015, doi:10.1029/2009GC002386.

Cadio, C., Ballmer, M.D., Panet, I., Diamen, M. & Ribe, N., 2012. New constraints on the origin of the Hawaiian swell from wavelet analysis of the geoid to topography ratio, *Earth planet. Sci. Lett.,* **359–360,** 40–54.

Chandrasekhar, S., 1961. Hydrodynamic and Hydromagnetic Stability, Dover, New York.

Choblet, G. & Sotin, C., 2000. 3D thermal convection with variable viscosity: can transient cooling be described by a quasi-static scaling law? *Phys. Earth planet. Inter.,* **119,** 321–336.

Courtillot, V., Jaupart, C., Manighetti, I., Tapponnier, P. & Besse, J., 1999. On causal links between flood basalts and continental breakup, *Earth planet. Sci. Lett.,* **166,** 177–195.

Crough, S.T., 1978. Thermal origin od mid-plate hot-spot swells, *Geophys. J. R. astr. Soc.,* **55,** 451–469.

Crough, S.T. & Thompson, G.A., 1976. Numerical and approximate solutions for lithospheric thickening and thinning, *Earth planet. Sci. Lett.,* **31,** 397–402.

Davaille, A. & Jaupart, C., 1993. Transient high-Rayleigh-number thermal convection with large viscosity variations, *J. Fluid Mech.,* **253,** 141–166.

Davaille, A. & Jaupart, C., 1994. Onset of thermal convection in fluids with temperature-dependent viscosity: application to the oceanic mantle, *J. geophys. Res.,* **99,** 19 853–19 866.

Detrick, R.S. & Crough, S.T., 1978. Island subsidence, hot spot, and lithospheric thinning, *J. geophys. Res.,* **83,** 1236–1244.

Doin, M.P., Fleitout, L. & Christensen, U., 1997. Mantle convection and stability of depleted and undepleted continental lithosphere, *J. geophys. Res.,* **102,** 2771–2787.

Dumoulin, C., Doin, M.P., Arcay, D. & Fleitout, L., 2005. Onset od small-scale instabilities at the base of the lithosphere: scaling laws and role of pre-existing lithospheric structures, *Geophys. J. Int.,* **160,** 344–356.

Fleitout, L. & Yuen, D., 1984. Secondary convection and the growth of oceanic lithosphere, *Phys. Earth planet. Inter.,* **36,** 181–212.

Gerya, T.V., Perchuk, L.L. & Burg, J.P., 2008. Transient hot channels: perpetrating and regurgitating ultrahigh-pressure, high-temperature crust–mantle associations in collision belts, *Lithos,* **103,** 236–256.

Gerya, T.V. & Yuen, D.A., 2003. Characteristics-based marker-in-cell method with conservative finite-differences schemes for modeling geological flows with strongly variable transport properties, *Phys. Earth planet. Inter.,* **140,** 293–318.

Gibert, B., Schilling, F.R., Gratz, F. & Tommasi, A., 2005. Thermal diffusivity of olivine single crystals and a dunite at high temperature: Evidence for heat transfer by radiation in the upper mantle, *Phys. Earth planet. Inter.,* **151,** 129–141.

Hirth, G. & Kohlstedt, D.L., 1996. Water in the oceanic upper mantle: implications for rheology, melt extraction and the evolution of the lithosphere, *Earth planet. Sci. Lett.,* **144,** 93–108.

Houseman, G.A., 1983. Large aspect ratio convection cells in the upper mantle, *Geophys. J. R. astr. Soc.,* **75,** 309–334.

Huang, J., Zhong, S. & Van Hunen, J., 2003. Controls on sublithospheric small-scale convection, *J. geophys. Res.,* **180**(B8), 2405, doi:10.1029/2003JB002456.

Jordan, T.H., 1979. Mineralogies, densities, and seismic velocities of garnet lherzolites and their geophysical implications, in *The Mantle Sample: Inclusions in Kimberlites and other Volcanics,* Vol. 2, pp. 1–14, eds Boyd, F.R. & Meyer, H.O.A., American Geophysical Union, Washington, DC.

Karato, S., 1986. Does partial melting reduce the creep strength of the upper mantle?, *Nature,* **319,** 309–310.

Katz, R.F., Spiegelman, M. & Langmuir, C.H., 2003. A new parameterization of hydrous mantle melting, *Geochem. Geophys. Geosyst.,* **4**(9), 1073, doi:10.1029/2002GC000433.

Korenaga, J. & Jordan, T.H., 2002. On the state of sublithospheric upper mantle beneath a supercontinent, *Geophys. J. Int.,* **149,** 179–189.

Korenaga, J. & Jordan, T.H., 2003. Physics of multiscale convection in Earth's mantle: onset of sublithospheric convection, *J. gheophys. Res.,* **108**(B7), 2333, doi:10.1029/2002JB001760.

Laske, G. *et al.*, 2011. Asymmetric shallow mantle structure beneath the Hawaiian Swell—evidence from Rayleigh waves recorded by the PLUME network, *Geophys. J. Int.,* **187,** 1725–1742.

Li, Y., Kind, R., Yuan, X., Wolbern, I. & Hanka, W., 2004. Rejuvenation of the lithosphere by the Hawaiian plume, *Nature,* **427,** 827–829.

Lodge, A. & Helffrich, G., 2006. Depleted swell root beneath the Cape Verde Islands, *Geology,* **34,** 449–452.

Manga, M., Weeraratne, D. & Morris, S.J.S., 2001. Boundary-layer thickness and instabilities in Bénard convection of a liquid with a temperature-dependent viscosity, *Phys. Fluids,* **13,** 802–805.

Monnereau, M., Rabinowicz, M. & Arquis, E., 1993. Mechanical erosion and reheating of the lithosphere: a numerical model for hotspot swells, *J. geophys. Res.,* **98,** 809–823.

Moore, W.B., Schubert, G. & Tackley, P.J., 1998. Three-dimensional simulations of plume-lithosphere interaction at the Hawaiian swell, *Science,* **279,** 1008–1011.

Olson, P., Schubert, G., Anderson, C. & Goldman, P., 1988. Plume formation and lithosphere erosion: a comparison of laboratory and numerical experiments, *J. geophys. Res.,* **93,** 15 065–15 084.
Morris, S. & Canright, D., 1984. A boundary-layer analysis of Benard convection in a fluid of strongly temperature-dependent viscosity, *Phys. Earth planet. Inter.,* **36,** 355–373.
Ribe, N.M., 2004. Through thick and thin, *Nature,* **427,** 793–795.
Ribe, N.M. & Christensen, U., 1994. Three-dimensional modeling of plume–lithosphere interaction, *J. geophys. Res.,* **99,** 669–682.
Richter, F.M., 1973. Convection and large-scale circulation of the mantle, *J. geophys. Res.,* **78,** 8735–8745.
Schmerr, N., 2012. The Gutenberg discontinuity: melt at the lithosphere-asthenosphere boundary, *Science,* **335,** 1480–1483.
Schutt, D.L. & Lesher, C.E., 2006. Effects of melt depletion on the density and seismic velocity of garnet and spinel lherzolite, *J. geophys. Res.,* **111,** B05401, doi:10.1029/2003JB002950.
Sleep, N.H., 1987. Lithospheric heating by mantle plumes, *Geophys. J. R. astr. Soc.,* **91,** 1–11.
Sleep, N.H., 1994. Lithospheric thinning by midplate mantle plumes and the thermal history of hot plume material ponded at sublithospheric depths, *J. geophys. Res.,* **99,** 9327–9343.
Sphon, T. & Schubert, G., 1982. Convective thinning of the lithosphere: a mechanism for the initiation of continental rifting, *J. geophys. Res.,* **87,** 4669–4681.
Solomatov, V.S. & Moresi, L.N., 2000. Scaling of time-dependent stagnant lid convection: application to small-scale convection on Earth and other terrestrial planets, *J. geophys. Res.,* **105,** 21 785–21 817.
Takei, Y. & Holtzman, B.K., 2009. Viscous constitutive relations of solid-liquid composites in terms of grain boundary contiguity: 1. Grain boundary diffusion control model, *J. geophys. Res.,* **114,** doi:10.1029/2008JB005850.
Thoraval, C., Tommasi, A. & Doin, M.P., 2006. Plume-lithosphere interaction beneath a fast moving plate, *Geophys. Res. Lett.,* **33,** doi:10.1029/2005GL024047.
Tommasi, A., Gibert, B., Seipold, U. & Mainprice, D., 2001. Anisotropy of thermaldiffusivity in the upper mantle, *Nature,* **411,** 783–786.
Van Hunen, J., Huang, J. & Zhong, S., 2003. The effect of shearing on the onset and vigor of small-scale convection in a Newtonian rheology, *Geophys. Res. Lett.,* **30,** doi:10.1029/2003GL018101.
van Hunen, J., Zhong, S.J., Shapiro, N.M. & Ritzwoller, M.H., 2005. New evidence for dislocation creep from 3-D geodynamic modeling the Pacific upper mantle structure, *Earth planet. Sci. Lett.,* **238,** 146–155.
Villagomez, D.R., Toomey, D.R., Hooft, E.E.E. & Solomon, S.C., 2007. Upper mantle structure beneath the Galapagos Archipelago from surface wave tomography, *J. geophys. Res.,* **112,** doi:10.1029/2006JB004672.
Wolfe, C.J., Solomon, S.C., Laske, G., Collins, J.A., Detrick, R.S., Orcutt, J.A., Bercovici, D. & Hauri, E.H., 2009. Mantle shear-wave velocity structure beneath the Hawaiian hot spot, *Science,* **326,** 1388–1390.
Wolfe, C.J., Solomon, S.C., Laske, G., Collins, J.A., Detrick, R.S., Orcutt, J.A., Bercovici, D. & Hauri, E.H., 2011. Mantle P-wave velocity structure beneath the Hawaiian hot spot, *Earth planet. Sci. Lett.,* **303,** 267–280.
Zaranek, S.E. & Parmentier, E.M., 2004. Convective cooling of an initially stably stratified fluid with temperature-dependent viscosity: implications for the role of solid state convection in planetary evolution, *J. geophys. Res.,* **109,** B03409, doi:10.1029/2003JB002462.
Zlotnik, S., Afonso, J.C., Díez, P. & Fernàndez, M., 2008. Small-scale gravitational instabilities under the oceans: implications for the evolution of oceanic lithosphere and its expression in geophysical observables, *Phil. Mag.,* **88,** 3197–3217.

APPENDIX A: LATERAL VARIATIONS OF BOUNDARY CONDITION IN THERMAL CONDUCTIVITY

In order to obtain the same lithosphere age at a fixed location within the box for any plate velocity, the thermal conductivity is increased in a narrow region in the leftmost part of the model, close to the ridge (upper left corner), whose width is labelled X_0 (Fig. A1) to accelerate the conductive cooling as the lithosphere moves away from the oceanic ridge. To obtain a lithosphere of given age t_1 at the constant location $X = X_0 + X_1$, the age of the lithosphere at X_0, t_0, must be adjusted by modifying the thermal conductivity k_0 in the X_0 wide domain in relation to the reference thermal conductivity, k, following the relationship:

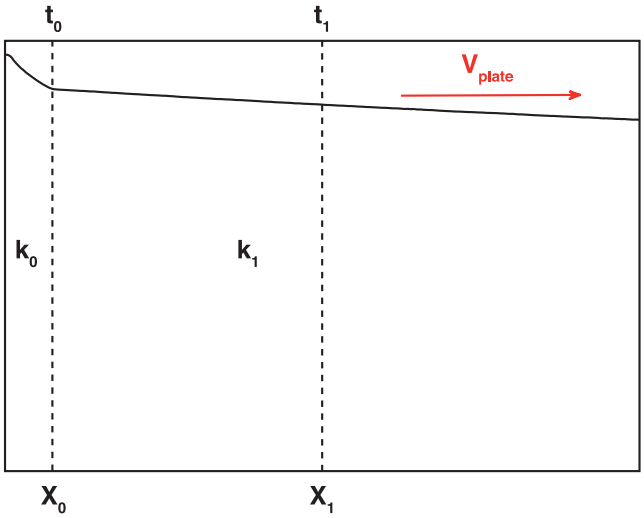

Figure A1. Sketch of the thermal boundary condition in conductivity used to reduce the box width.

$$\begin{aligned} \sqrt{k_0 \tfrac{X_0}{V_{\text{plate}}}} &= \sqrt{k t_0} \\ t_0 &= t_1 - \tfrac{X_1}{V_{\text{plate}}} \end{aligned}, \tag{A1}$$

where V_{plate} is the plate velocity. Rearranging eq. (A1), the thermal conductivity κ_0 is increased according to

$$k_0 = k\left(t_1 - \frac{X_1}{V_{\text{plate}}}\right)\frac{V_{\text{plate}}}{X_0}. \tag{A2}$$

The approximation (A2) does not only increase the vertical heat flow, producing as desired a faster ageing of the lithosphere, but it also increases the horizontal heat flow, by both directly increasing the thermal conductivity and significantly shortening the horizontal length scale. Such an enhanced horizontal heat flow might distort the half-space lithosphere cooling in the whole box. To verify the effect of the approximation (A2) had outside the domain in which it was applied, we compared the thermal lithosphere structure of a fast-moving plate in a model with a constant thermal conductivity against the equivalent model using the condition (A2), with a reduced box width of 2000 km.

We performed two simulations with a plate velocity, V_{plate}, of 10 cm yr^{-1} and mantle background viscosities, μ_1, of 5×10^{20} and 10^{20} Pa s. The boundary conditions used are the same as described in the main text. We compare the lithosphere structure at an age, t_1, of 40 Myr, using a box 6000 km wide box where the approximation (A2) is not take into account, and a 4000 km wide box when the thermal conductivity is modified in the first 150 km of the model, producing a lithosphere structure at 2000 km away from the ridge that is similar to the one simulated at 4000 km away from the ridge in the model where the condition (A2) is not imposed. Fig. A2 shows the lithosphere thermal state obtained in the two models with and without thermal conductivity increasing. The horizontal heat flux close to the left side of the box, where the thermal conductivity is increased, is effectively higher than in the case where the

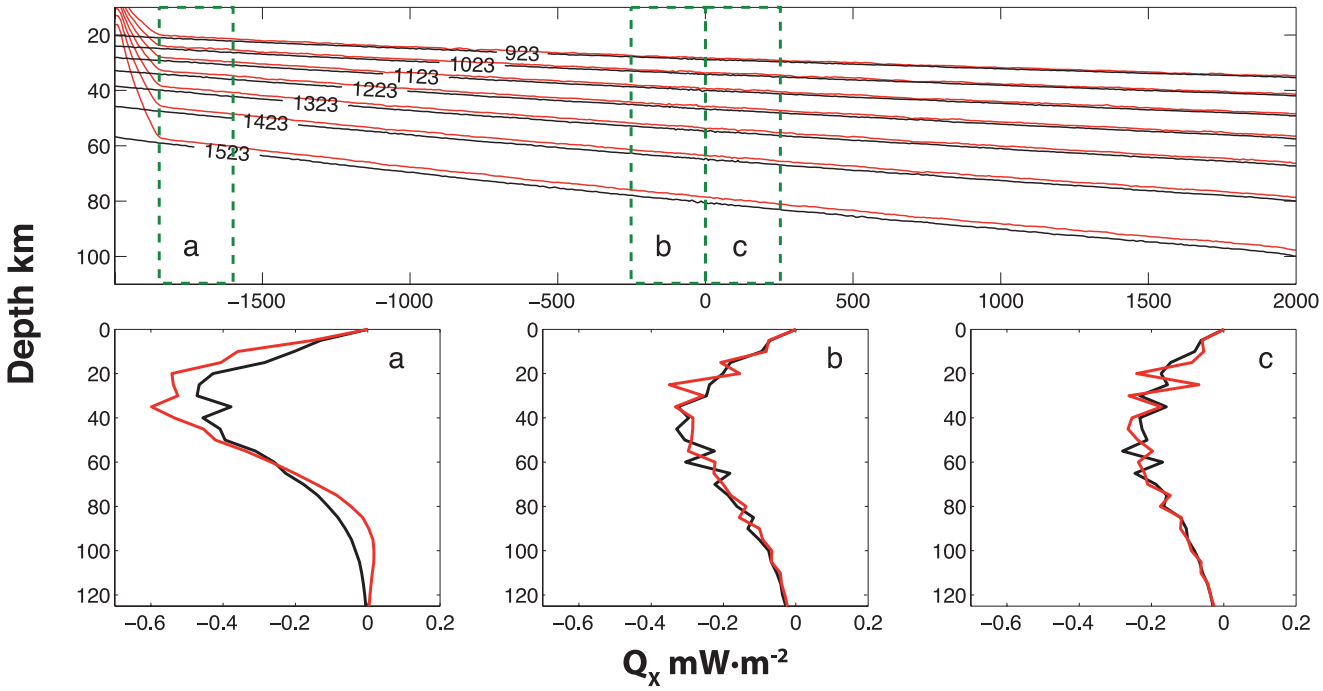

Figure A2. Comparison between lithosphere thermal structures obtained for a lithosphere cooling accelerated in a narrow region close to the ridge (red line) and for a normal lithosphere cooling (black line). (Top) Isotherm contours for the two models. (a)–(c) Vertical profiles of horizontal heat flux in three different regions of the box, indicated by the rectangles delimited by the dashed green line in the top figure.

approximation (A2) is not included (Fig. A2a). However, far away from the modified conductivity domain, average horizontal heat fluxes in the two models vary by less than 2 per cent (Figs A2b and c). In other words, accelerating the diffusion process at the beginning of the lithosphere cooling does not significantly affect the cooling of the lithosphere in the area where the plume impinges and interacts with its base. The only notable difference is the slightly younger lithosphere age, as isotherms are ∼2 km shallower, in the case of the reduced model, possibly indicating a slightly too increased diffusivity.

We also tested if the faster ageing of the lithosphere affects the development of the SSC by comparing the onset time of SSC and the lithosphere erosion. Fig. A3 shows a plume generated by a thermal anomaly of 200 K, impinging the lithosphere (simulation 7, Table 2). The time–space plots (Figs A3c and d) of the temperature computed at the sublithospheric depth (87 km) show approximately the same location of the plume impact point and the location of the first dripping instability. The values of the impact point, first dripping instability, and dimensionless onset time of SSC, averaged on the steady state window time, are listed in Table A1, for simulations 7 and 35 (Table 2). The difference is negligible, less than 3 per cent for a weaker plume and up to 5 per cent for a more vigorous plume (simulation 7, difference between X_{onset} and X_{impact} is 16 km). The lithosphere erosion also does not seem to be affected by the boundary condition in thermal conductivity (Fig. A4). The condition (A2) is thus satisfying for decreasing the width of the simulation box for models with fast plate velocities. It allows for using a unique model setup to produce similar thermal lithosphere structures for different plate velocities.

APPENDIX B: RESOLUTION TESTS

We performed numerical simulations to test the influence of the grid resolution on the plume dynamics when a plume rises through an upper mantle with a pressure- and temperature-dependent viscosity. The resolution parameters investigated are: (1) the size of the Eulerian mesh; (2) the density of Lagragian markers used to interpolate rock properties and time-evolving variables (temperature, stress, strain rate, etc.) from Eulerian nodes back to markers; (3) the maximum allowed marker displacement (Δs) in the advection scheme to adjust the time step. To ensure stability of numerical solution, the time step, $\Delta t = \Delta s(L/V)$, where L is the mesh size and V is the maximum velocity in the box, should be sufficiently small to prevent any markers material from moving over more than one mesh unit per time step.

Simulations were computed on a 700 × 700 km box discretized using a rectangular grid, with the finest resolution imposed on a 250 ± 10 km domain, defined from the top and located horizontally in the middle of the box where the plume rises (Fig. 1a). A fluid with a homogeneous peridotite composition fills the box. The viscosity at the bottom of the box (700 km depth) is set to 5×10^{20} Pa s, the smaller viscosity used in the plume–lithosphere interactions simulations.

Mechanical boundary conditions are free slip on all sides, except for the bottom, which is a semi-natural open boundary (external no slip boundary condition, see main text for definition). The initial thermal structure of the lithosphere is laterally uniform, corresponding to 40 Myr old oceanic lithosphere, with a temperature of 1573 K at 90 km depth. The bottom of the box has a constant temperature $T_1 = 1623$ K and the surface temperature is set to 273 K. The plume anomaly diameter at the box bottom is of 50 km with a temperature of 1973 K. This setup induces a very low viscosity in the plume body (∼7×10^{17} Pa s at 130 km depth) and, as a consequence, high rising velocities (around 150 cm yr^{-1} at 250 km depth). The performed resolution tests are presented in Table B1.

We used the simulation computed on the finest resolution (3 km × 6 km) as a reference to evaluate the results obtained on coarser meshes. There is, however, a trade-off between meshes with

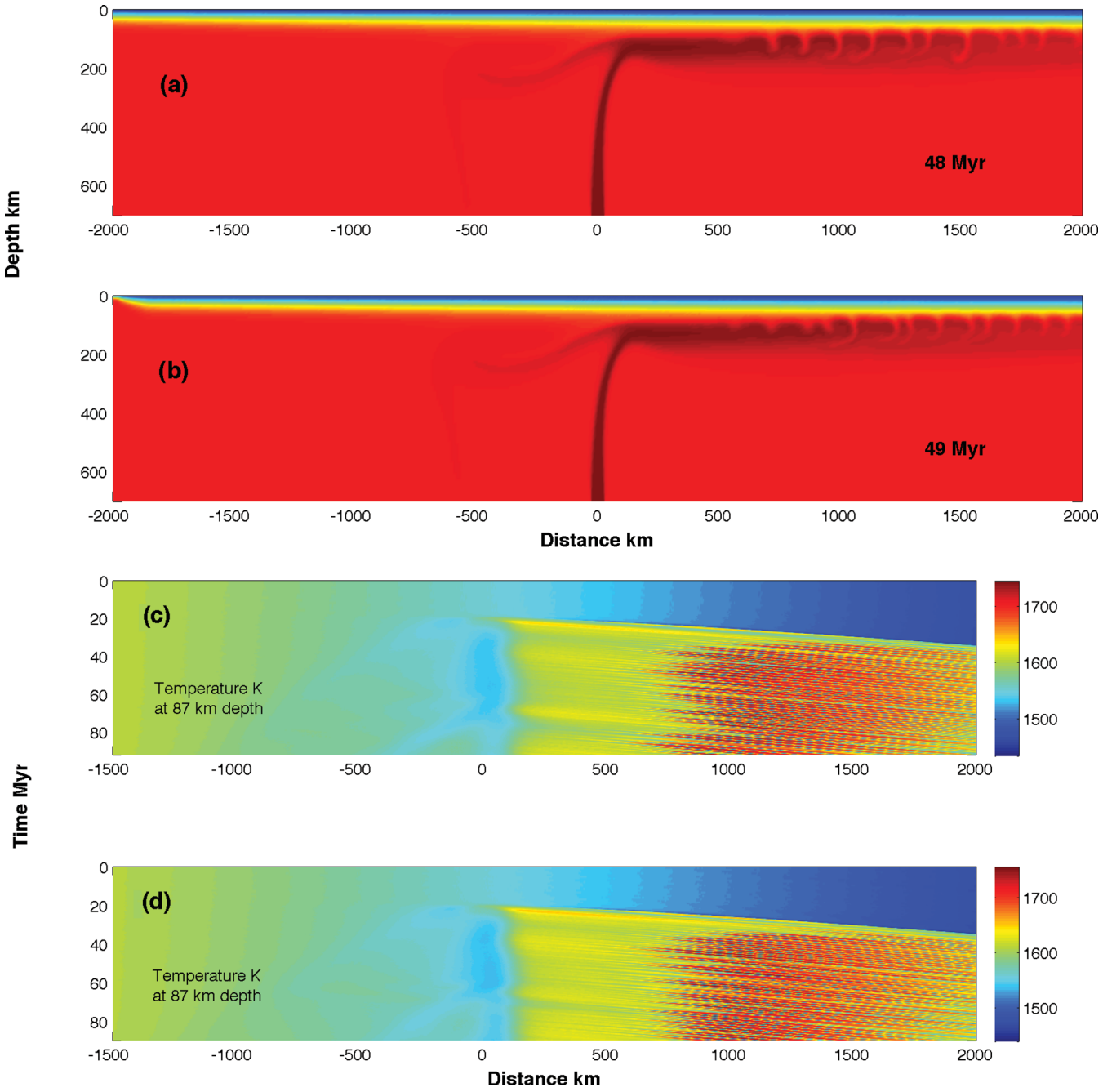

Figure A3. The simulation 7 (Table 2) of a plume generated by a thermal anomaly ΔT_{plume} of 200 K impinging a plate moving at 10 cm yr^{-1}, computed without using the approximation (A2) (a) and using it (b). (c) and (d) represent the time–space plots of the temperature of the simulations (a) and (b), respectively, computed at the sublithospheric depth of 87 km. The two plots show similar locations of the plume impact and begin of the SSC convection between the models.

Table A1. List of the locations of the impact point, X_{impact}, and first drip instability, X_{onset}, and dimensionless onset time of the SSC. For the two models tested.

	Box reduction	X_{impact} Km	X_{onset} km	$t_c/(H^2/\kappa)$
μ_1 5 × 10^{20} Pa s	YES	107.6	616.6	2.543 × 10^{-4}
$\Delta T_{\text{plume}} = 200$ K	NO	107.7	632.0	2.619 × 10^{-4}
μ_1 10^{21} Pa s	YES	25.0	326.9	1.508 × 10^{-4}
$\Delta T_{\text{plume}} = 350$ K	NO	37.4	324.8	1.436 × 10^{-4}

different resolutions and it was not possible to simulate exactly the same plume state in all models, with small variations both in elapsed time and plume shape (Figs B1e and f). Two criteria have been considered to select times for comparing simulations with different resolutions: (1) when the plume head reaches the depth of 450 km (simulations labelled as *a* in Figs B1a and c) and (2) when the plume head reaches a width of 500 km at the base of the lithosphere (simulations labelled as *b* in Figs B1c and d).The dependence of the solution on the Eulerian mesh has been tested by increasing the cell size, but keeping constant the ratio between the smallest and the largest sizes (equal to 0.5). We tested cell sizes of 3 × 6, 4 × 8, 5 × 10 and

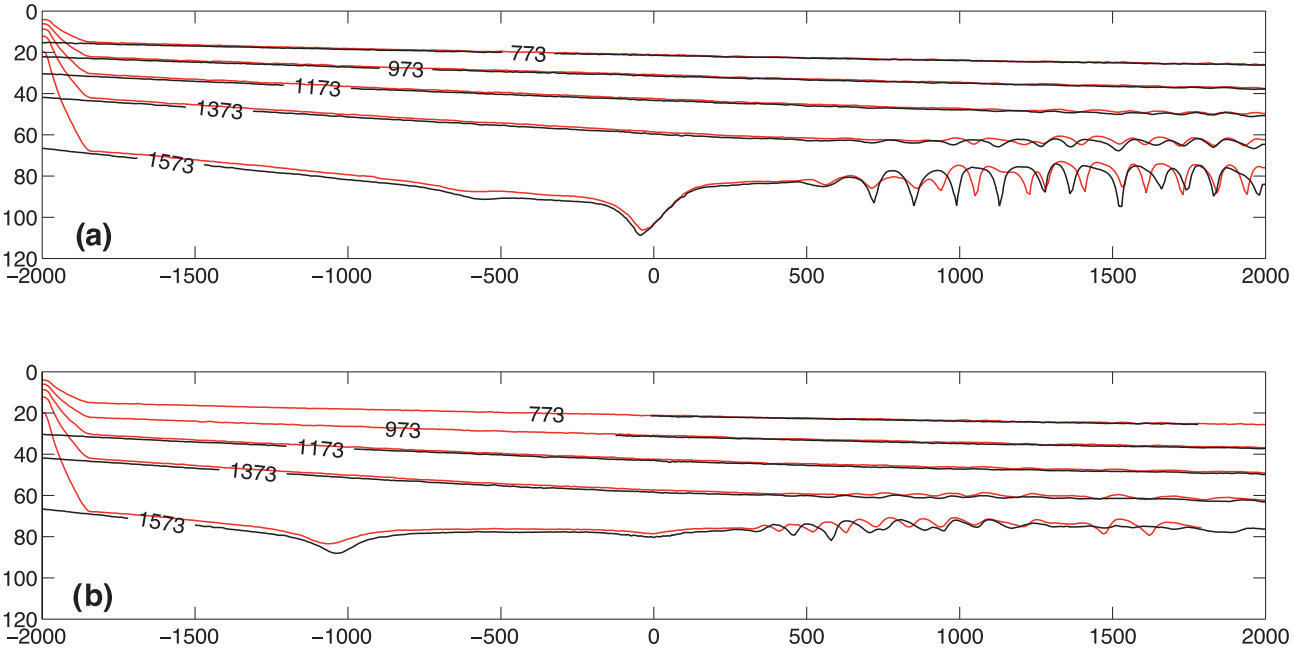

Figure A4. Comparison between lithosphere thermal structures modified by the presence of the plume, obtained for a lithosphere cooling accelerated in a narrow region close to the ridge (red line) and for a normal lithosphere cooling (black line). (a) The simulation 7 (Table 2) of a plume generated by a thermal anomaly ΔT_{plume} of 200 K, and (b) by a thermal anomaly ΔT_{plume} of 350 K (simulation 35, Table 2), both impinging a plate moving at 10 cm yr^{-1}.

Table B1. Numerical setups used in the resolution tests.

Simulation	Eulerian Node X, Y	Marker in the smallest cell	Markers number
3 × 6	167 160	16	670 000
4 × 8	126 122	16	390 000
5 × 10 single	101 96	16	340 000
6 × 12	8581	16	240 000
5 × 10 double	101 96	64	1 370 000

6 × 12 km^2. The root mean square (rms) temperature computed all over the box is not significantly affected by changes in the mesh size; the error is less than 0.5 per cent. The velocity field is more dependent on the mesh resolution, but the error never overruns 6 per cent (Fig. B2a).Marker density effects were tested by considering a denser model (double in Fig. B2b) against the less dense one (single in Fig. B2b). A higher number of markers increase the interpolation quality on Eulerian nodes. The initial marker distribution for the denser model (double) corresponds to ∼1170 markers distributed in horizontal and vertical directions every 0.6 km, the smallest cell (5 × 5 km^2) containing 64 markers. For the less dense model (single), there are ∼590 markers every 1.2 km in each direction, with a total 16 markers in smallest cell. The total number of markers is listed in Table A1. The error in rms values due to a less dense marker distribution is very low, less than 1 per cent (Fig. B2b).

At last we tested the effect of the maximum allowed marker displacement (Δs) considering values of 0.15, 0.3 and 0.5. For numerical accuracy, Δs must not be higher than 0.5. The rms temperature computed all over the box is not influenced by Δs in the range tested (error less than 0.1 per cent). The velocity field is more sensitive to Δs value. We estimate a maximum error of 2 per cent for the test performed with $\Delta s = 0.3$. The error increases for the $\Delta s = 0.5$ case attaining 5 per cent (Fig. B2c).

Considering the present results and the associated computation time, the numerical resolution with a mesh of 5 × 10 km, Δs set to 0.3 and, a marker distribution with 16 in the cell, was defined as the best compromise to simulate the plume–lithosphere interactions.

Moreover, a supplementary test has been performed to verify if the vertical resolution in the upper part of the box may affect the cooling of the plume material that spreads at the bottom of the lithosphere and the penetration of the cold sublithospheric instabilities into the asthenosphere. Different refinement schemes applied to the same region have been compared, using a refined grid, with a 5 km high and 10 km wide mesh extended up to 250 km or to 350 km depth. The two simulations show the same thickness of the hot plume material pancake at the base of the lithosphere and the same amplitude of SSC blob dripping (Fig. B3).

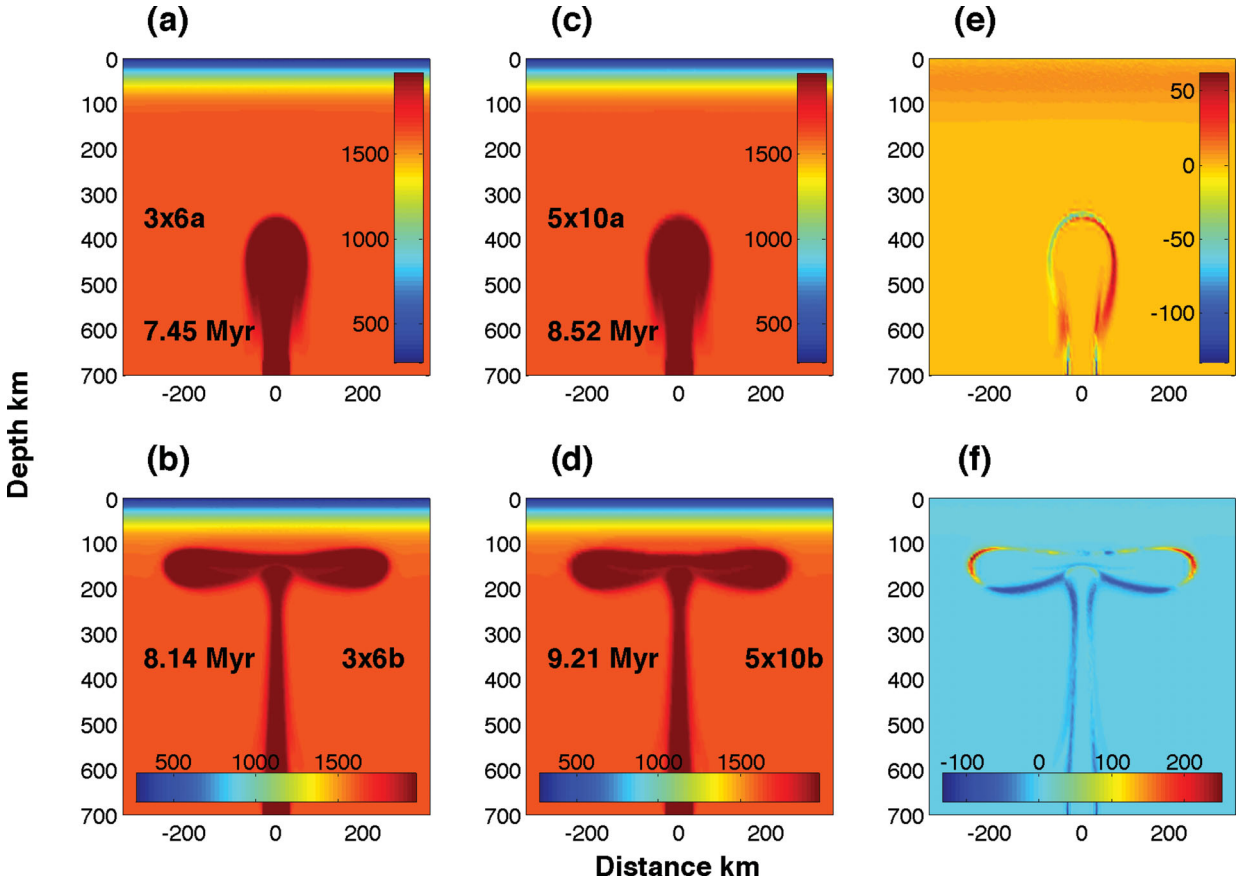

Figure B1. Example of resolution test. (a, c and e) and (b, d and f) display the two times analysed. (a, b) and (c, d) show the temperature field for models with a 3 × 6 km and a 5 × 10 km mesh, respectively. (e, f) column shows the difference in the temperature field between the two models.

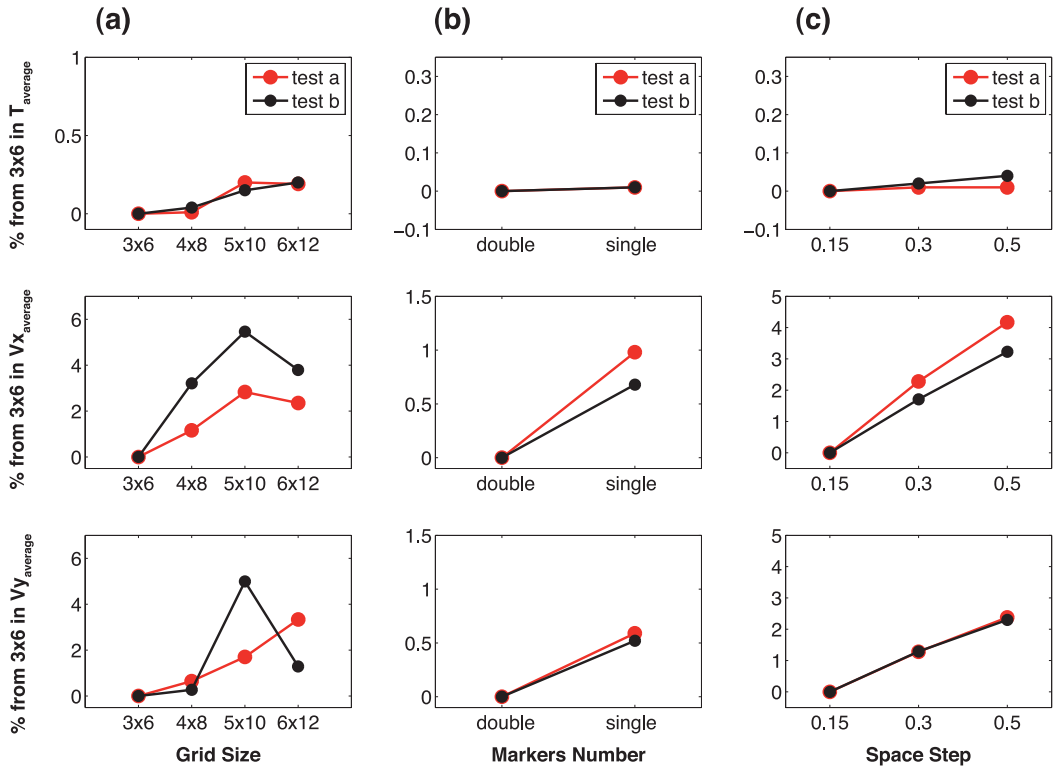

Figure B2. Percentage shift from the rms of temperature, horizontal and vertical velocity of the model computed for different grid sizes (a), markers density (b) and different maximum allowed marker displacement (c).

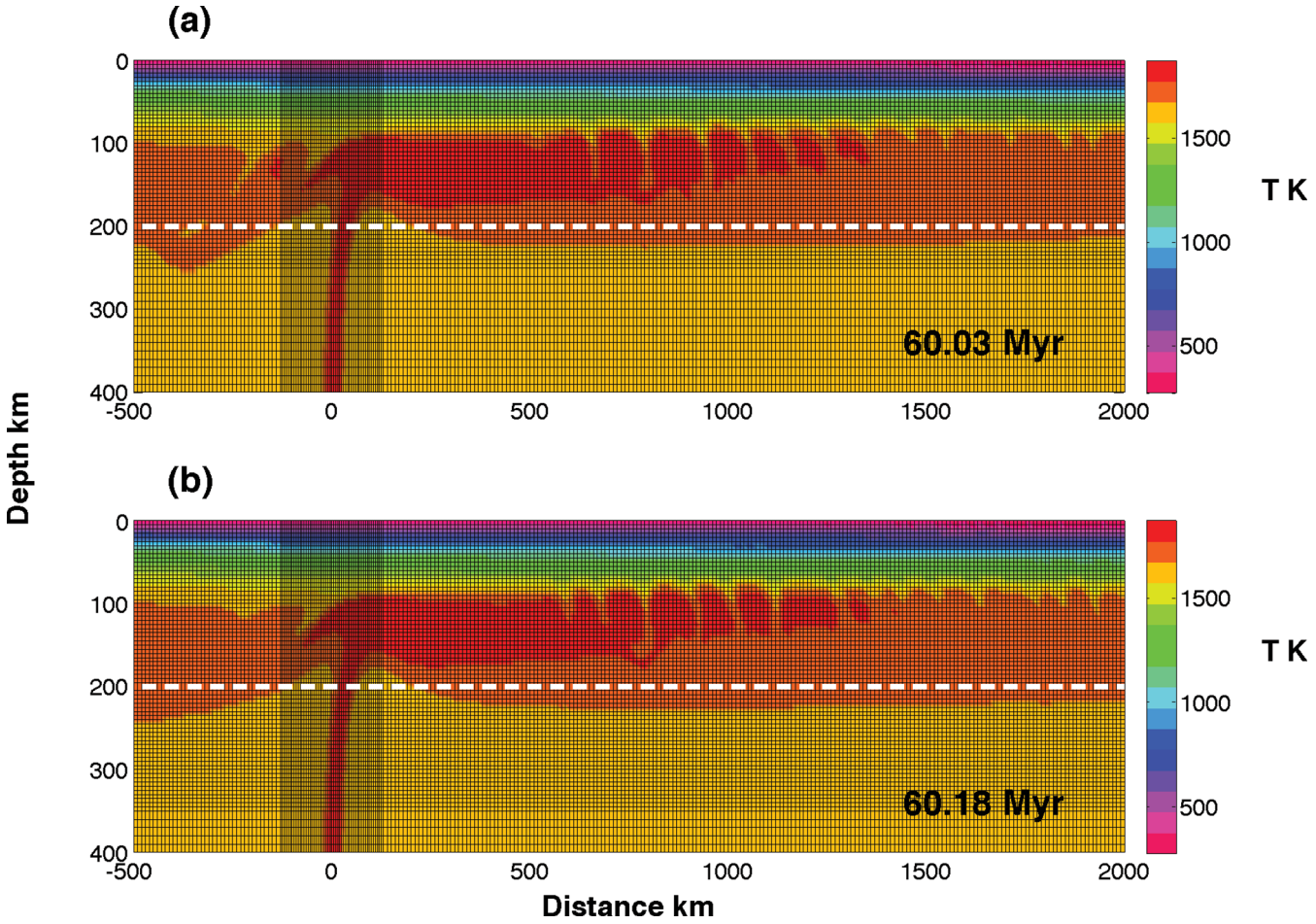

Figure B3. Simulations for a plume generated by a thermal anomaly of 250 K, impinging a plate moving at 7.5 cm yr^{-1}, with a mantle viscosity of 7.5 $\times$ 10^{20} Pa s (simulation 14, Table 2). The two simulations are computed with a refined vertical resolution in the upper part of the box up to 250 km (a) and to 350 km (b) depth. The thickness of the pancake formed by the lateral spreading of the plume material and the depth of penetration of the cold instabilities in the lower part are similar in both cases. The dashed white lines indicate the depth of 200 km. The colour map indicates the temperature in Kelvin.